Journal of Environmental Management 410 (2026) 130074

Contents lists available at ScienceDirect

Journal of Environmental Management

journal homepage: www.elsevier.com/locate/jenvman

Research article

Engineering Bi_3O_4Br/TiO_2 nanobelt/glucose hydrochar heterostructures for enhanced visible-light degradation of pharmaceutical pollutants

Sajad Ahmadi [a], Antonio Alonso [b], Velma Beri Kimbi Yaah [c], Sergio Botelho de Oliveira [d], Rafal Sliz [e], Satu Ojala [a,*]

[a] Environmental and Chemical Engineering, Faculty of Technology, University of Oulu, Oulu, Finland
[b] Instituto de Física, Universidade Federal de Goiás, Goiânia, Brazil
[c] Nano and Molecular Systems Research Unit, University of Oulu, P.O. Box 4500, FI, 90014, Finland
[d] Department of Chemistry, Federal Institute of Goiás, Goiania, 74055 110, Brazil
[e] Optoelectronics and Measurement Techniques Unit, University of Oulu, P.O. Box 4500, FI, 90014, Finland

ARTICLE INFO

Keywords:
Glucose hydrochar
Photocatalysis
Paracetamol
TiO_2 nanobelts
Bi_3O_4Br

ABSTRACT

The existence of pharmaceutical residues, such as paracetamol, in water bodies is extremely risky to the environment and human health, and thus efficient and sustainable remediation technologies should be developed. In this study, a novel ternary Z-scheme photocatalyst consisting of bismuth-rich oxybromide (Bi_3O_4Br), TiO_2 nanobelts (TiO_2 NB), and glucose-derived hydrochar (GH) was synthesized to degrade paracetamol under visible light irradiation. The effect of the synthesis procedure was explored through a two-step and one-step hydrothermal synthesis method. The photocatalyst prepared with the two-step procedure showed better efficiency and the increased growth of Bi_3O_4Br nanosheets around the hydrochar, resulting in better interface electronic coupling and charge separation efficiency compared to the synthesized one-step material and Bi_3O_4Br/TiO_2 NB heterostructure. Photocatalytic experiments showed that the two-step 10% composite displayed the highest paracetamol degradation efficiency of approximately 91% at natural pH, outperforming the pristine TiO_2 NB, Bi_3O_4Br, and the Bi_3O_4Br/TiO_2 NB heterostructure photocatalyst under visible light irradiation. Scavenger tests and electron paramagnetic resonance (EPR) analysis revealed the role of the reactive species (h^+, •OH, and O_2•$^-$) during the photocatalytic tests, indicating the primary contributions of holes and superoxide radicals and the minor contribution of hydroxyl radicals. The Z-scheme mechanism was also proven by selective photodeposition of Pt and MnO_x. The photocatalysts remained active during five cycles of photocatalytic experiments and demonstrated potential for treating real pharmaceutical wastewater, indicating their promising application in the sustainable remediation of pharmaceutical wastewater.

1. Introduction

Photocatalysis refers to a light-induced chemical process in which a photocatalyst absorbs photons to trigger redox reactions that degrade pollutants into less harmful or mineralized forms. Its efficiency depends on catalyst characteristics, pollutant concentration, light intensity, and environmental factors, such as pH and temperature (Nannou et al., 2025; Zeinali et al., 2025). As an advanced oxidation process (AOP), photocatalysis offers clear advantages over conventional treatments like adsorption, which merely transfer contaminants from one phase to another. It decomposes completely persistent pollutants through the formation of highly reactive oxygen species (ROS), including hydroxyl and superoxide radicals. This approach operates under ambient conditions and utilizes solar energy as a renewable energy source (Wu et al., 2025; Yang et al., 2025; Quimbayo et al., 2025). When irradiated, the semiconductor photocatalyst generates electron-hole pairs, but the rapid recombination of these charge carriers limits efficiency (Bertagna Silva and Marques, 2025; Sun et al., 2025; Ahmadi et al., 2025a). To address this, various modification strategies, such as doping, defect engineering, and heterojunction design, have been developed. Among these, Z-scheme heterojunctions are particularly effective, as they selectively preserve the most reactive electrons and holes, enhancing redox performance (Bertagna Silva and Marques, 2025; Li et al., 2025a, 2025b). Although significant progress has been achieved, challenges remain,

* Corresponding author.
E-mail addresses: sajad.ahmadi@oulu.fi (S. Ahmadi), satu.ojala@oulu.fi (S. Ojala).

https://doi.org/10.1016/j.jenvman.2026.130074
Received 24 March 2026; Received in revised form 20 May 2026; Accepted 24 May 2026
Available online 30 May 2026

including short radical lifetimes. Continued development of efficient photocatalysts and system designs is essential to advance photocatalysis as a practical and sustainable method for the degradation of organic pollutants (Nannou et al., 2025; Sun et al., 2025; Lin et al., 2025; Kimbi Yaah et al., 2025; Ye et al., 2024, 2026).

The increasing presence of pharmaceutical residues in aquatic environments has become a significant environmental concern due to their persistence and potential risks to ecosystems and human health (Mukheef et al., 2024; Tabieh et al., 2025; Ahmed et al., 2025; Aljerf, 2018a). Among these contaminants, paracetamol is widely detected in wastewater and surface waters due to its extensive consumption and incomplete removal in conventional treatment systems (AlJerf et al., 2026; Aljerf, 2018b; Hansen et al., 2025; Kaur and Pal, 2025). Consequently, development of efficient and sustainable treatment technologies is essential for mitigating pharmaceutical pollution and improving water quality. Light-emitting diodes (LEDs) have recently gained prominence as an efficient alternative to conventional light sources in photocatalytic systems. Unlike mercury or xenon lamps, LEDs combine high energy efficiency, long lifespan, low heat output, and compact design with environmental safety and low operating costs (Li et al., 2022; Khodadadian et al., 2018). Their small size allows flexible reactor configurations, enhancing overall process efficiency. Owing to the advantages, LEDs have proven highly effective in driving photocatalytic degradation of organic pollutants and represent a promising source of illumination for advanced environmental remediation technologies.

Titanium dioxide (TiO_2) is one of the most widely studied photocatalysts due to its stability, low cost, and non-toxicity (Asghar et al., 2025). TiO_2 nanobelts (TiO_2 NB) have gained attention for photocatalytic applications due to their one-dimensional morphology, which provides a high surface area and efficient charge transport along the axial direction (Meng et al., 2025; Ahmadi et al., 2024a). However, its practical application is limited by its wide band gap and rapid recombination of photogenerated charge carriers. To overcome these limitations, various strategies, such as heterojunction construction and incorporation of carbon-based materials have been explored to enhance visible-light activity and charge separation efficiency. Bi-rich bismuth oxybromides photocatalysts, such as Bi_3O_4Br have been developed by tuning the Bi stoichiometry, which effectively adjusts the electronic band structure and enhances charge carrier dynamics (Zhang et al., 2025a). Bi_3O_4Br has a moderate bandgap (2.3-2.7 eV) that enables efficient absorption of visible light while maintaining good photostability (Wang et al., 2025; Niu et al., 2025). Its layered and non-stoichiometric structure facilitates charge separation and suppresses electron-hole recombination relative to stoichiometric BiOBr (Niu et al., 2025). These characteristics make it an interesting material to be combined with TiO_2 nanobelts.

Hydrochar, a carbonaceous material derived from biomass via hydrothermal carbonization (HTC), has recently gained attention as an efficient and sustainable component in photocatalytic systems. Unlike biochar produced through high-temperature pyrolysis, hydrochar is synthesized under moderate conditions (180-260 °C, 2-6 MPa) in an aqueous medium (Li et al., 2022; Zhang et al., 2024). This process yields a material rich in structural defects and oxygen-containing functional groups such as hydroxyl, ether, and carboxyl moieties. These surface functionalities enhance chemical reactivity, facilitate electron transfer, and in some cases promote the generation of reactive oxygen species (ROS), all of which are essential for photocatalytic redox processes (Zhou et al., 2019; Dong et al., 2025). While biochar has been extensively utilized as a conductive scaffold or electron mediator in semiconductor-based photocatalysts, the potential of hydrochar in similar applications has only recently started to be explored. The synthesis of carbon materials, such as activated carbon or biochar require drying of raw materials before process, high temperatures, and in some cases activating agents, such as KOH or H_3PO_4, whereas the synthesis of hydrochar requires less energy and is compatible with moisture-containing feedstocks, such as biogas digestate (Yadav et al., 2024). The abundant oxygenated surface groups on hydrochar can act as electron shuttles, promoting efficient interfacial charge transfer between semiconductor surfaces and reactant molecules (Li et al., 2022; Dong et al., 2025; Nor and Amin, 2019). Moreover, hydrochar could improve the stability and durability of semiconductor photocatalysts (Yadav et al., 2024). Hydrochar has demonstrated considerable potential in forming high-performance photocatalytic composites, such as HC/TiO_2 (Zhang et al., 2024), Fe_3O_4/BiOBr/HC (Li et al., 2022), AgBr/Bi_2WO_6/HC (Dong et al., 2025), and Bi_2WO_6/TiO_2/HC (Qi et al., 2023) showing enhanced photocatalytic efficiencies compared with their pristine counterparts, primarily due to hydrochar's ability to promote charge separation, extend visible-light absorption, and enhance pollutant adsorption at the catalyst interface.

While photocatalytic materials have advanced during the past years, their application in real-world environmental systems remains a major challenge. Many reported studies rely on high-energy UV sources and certain pH conditions. Therefore, there is a growing need for photocatalysts that can operate efficiently under visible light and near-neutral pH. In this context, the development of energy-efficient and environmentally relevant photocatalytic systems is essential for advancing water treatment technologies. Herein, for the first time, we report the ternary Z-scheme Bi_3O_4Br/TiO_2 nanobelt/glucose hydrochar (Bi_3O_4Br/TiO_2 NB/GH) photocatalyst and systematically illustrate the crucial role of the synthesis method on the structure, charge transfer process, and photocatalytic activity. Unlike previous research efforts that mainly concentrated on the composition of the photocatalysts, this study not only explores the importance of the one-step versus two-step hydrothermal method but also explores the importance of the glucose hydrochar in photocatalysis. Different ratios (5%, 10%, 15%, and 20%) of the glucose hydrochar were utilized to synthesize the Bi_3O_4Br/TiO_2NB/GH. The materials were comprehensively characterized. Additionally, the effect of parameters, such as pH, temperature, concentration, and photocatalyst dosage, on the degradation of paracetamol was investigated. Active species trapping experiments, EPR studies, and selective photo-deposition of Pt and MnO_x were conducted to elucidate the photocatalytic mechanism and charge carrier migration. The reusability of the Bi_3O_4Br/TiO_2 NB/GH were also assessed across four cycles. The performance of Bi_3O_4Br/TiO_2 NB in degrading real pharmaceutical wastewater was also evaluated.

2. Experimental section

2.1. Synthesis of Bi_3O_4Br/TiO_2 NB/GH (one-step vs two-step)

The detailed procedure for the synthesis of Bi_3O_4Br, TiO_2 NB, and Bi_3O_4Br/TiO_2 NB is described in our previous studies (Ahmadi et al., 2024b, 2025b). The photocatalyst containing glucose hydrochar was synthesized by the addition of different amounts of glucose precursor in order to have glucose hydrochar in the final product. Various amounts of glucose (5, 10, 15, and 20 W %) were added during the synthesis of the Bi_3O_4Br/TiO_2 NB heterojunction. A certain amount of glucose (according to each ratio) was added to 20 mL of MQ water and stirred for 15 min. The glucose solution was added to the mixture of Bi_3O_4Br precursors (2 mmol of $Bi(NO_3)_3{\cdot}5H_2O$ in 10 mL of ethylene glycol + 2 mmol of KBr in 10 mL of ultra-pure Milli-Q water) and the as-prepared TiO_2 NB before adding the NH_4OH. The mixture was stirred for 20 min and then 5 mL of NH_4OH was dropped into the solution in order to get the Bi_3O_4Br in final product. Finally, the mixed solution was transferred into an autoclave and heated at 160 °C for 18 h, followed by multiple washing cycles with ethanol and MQ water. Then, the sample was dried at 80 °C for 24 h. The samples synthesized in this method were labelled as one-step materials.

Another method was also used to synthesize these photocatalysts which was the two-step hydrothermal process. First, different amounts of glucose (5, 10, 15, and 20 W %), which were exactly the same as the

one-step method, were added to 20 mL of MQ water. Then, the as-prepared TiO_2 NB were added to glucose solution and hydrothermally treated at 180 °C for 12 h. Then, the obtained material was washed thoroughly and dried at 80 °C overnight. In the next step, 2 mmol of Bi $(NO_3)_3{\cdot}5H_2O$ was stirred in 10 mL of ethylene glycol until a clear solution formed. Then, 2 mmol of KBr was stirred into 10 mL of Milli-Q water. The two solutions were then combined to produce a white suspension, and the previously prepared TiO_2 NB/GH was added to this mixture. After stirring for 30 min, the mixture was transferred into an autoclave and heated at 160 °C for 18 h. The final product was obtained after thoroughly washing with ethanol and MQ water as well as drying at 80 °C for 24 h. The synthesized materials were labelled as two-step photocatalysts.

2.2. Characterization and EPR methodology

Structural analysis was performed using a Rigaku MiniFlex X-ray diffractometer (Co anode). Diffraction patterns were recorded over a scan range of 5-90° (2θ) and a step size of 0.02°. X-ray photoelectron spectroscopy (XPS) measurements were carried out on a Thermo Fisher Scientific ESCALab 250Xi, and the data were processed with ThermoAvantage™ software. All binding energies were referenced to the C1s peak at 284.8 eV. Sample morphology was examined using a Zeiss Ultra Plus FESEM equipped with an EDX detector. Platinum or carbon coating was applied to prevent charging depending on the materials. Transmission electron microscopy (TEM) was conducted using a JEOL JEM-2200FS EFTEM/STEM microscope. Nitrogen adsorption-desorption analyses were performed on Micromeritics ASAP 2020 to determine BET surface area, pore size, and pore volume. Prior to measurement, samples were degassed under vacuum at 120 °C for 720 min, followed by nitrogen sorption at −196 °C. Pore characteristics were evaluated using the BJH method. FTIR spectra were collected with a Bruker Vertex v80 spectrometer coupled to a Harrick Praying Mantis DRIFT unit, covering 400-4000 cm^{-1}. Raman spectra were obtained with a Timegated® 532 Pico Raman spectrometer (Timegate Instruments, Oulu, Finland), using 50% laser power to avoid sample alteration, and processed using Shsqui Matlab® software. Elemental composition was assessed with a PANanalytical® AXIOS mAX 4 kW XRF spectrometer with Omnian semi-quantative programme and a LECO CS-200 carbon sulphur analyser with loose powder method. UV-Vis diffuse reflectance spectra were recorded using a SHIMADZU UV-2600. The Kubelka-Munk method was applied to estimate the band gap energies of the photocatalysts (Equation (1)).

$$\left(hv \times F(R) = (Ahv - Eg)^{n/2}\right) \quad (1)$$

In this equation, F(R) represents the Kubelka-Munk function, h denotes Planck's constant, and ν is the frequency of the incident light. A is a proportionality constant, while Eg corresponds to the band gap energy. The value of n depends on the type of optical transition, with $n = 1$ used for direct transitions and $n = 4$ for indirect transitions. Electrochemical measurements were performed using a Metrohm Vionic system, with data acquisition and analysis completed through the Intello software package. The powdered materials were pressed between two electrodes at a pressure of 200 kgf cm^{-2}. Impedance data were recorded using a 10 mV perturbation over a frequency range of 2 MHz to 0.1 Hz, and the results were displayed as Nyquist plots. Photoluminescence (PL) spectra were collected with a Horiba Fluorolog-QM spectrometer, using a 250 nm excitation source. Emission spectra were measured from 330 to 750 nm at 1 nm steps with an integration time of 1 s. All analyses were carried out under identical experimental conditions.

The chemicals used for EPR measurement are 5,5-dimethyl-1-pyrroline-N-oxide (DMPO) and 2,2,6,6-Tetramethyl-4-piperidone 95% (TEMP), 2,2,6,6-Tetramethylpiperidine 1-oxyl, 2,2,6,6-Tetramethyl-1-piperidinyloxy 98% (TEMPO) were purchased from Sigma-Aldrich (St. Louis, MO, USA). EPR measurements were carried out on a Bruker EMX Plus spectrometer (Rheinstetten, Germany) under the following conditions: microwave frequency, 9.83 GHz; microwave power, 20 mW; modulation frequency, 100 kHz; modulation amplitude, 0.5 G; magnetic field scan, 60 or 80 G; sweep time, 168 s; and sample temperature, 25 °C. Irradiation experiments were performed using a visible light source (Br. Patent: PI 0802369-7 A2, 2008) equipped with a 500 W halogen lamp, delivering an energy dose of 720 J cm^{-2}, as previously described (Gonçalves et al., 2020; Alonso et al., 2016). To avoid sample heating, the light beam was passed through a water filter of sufficient thickness to absorb infrared radiation. The samples consisted of 100 μL of aerated photocatalyst suspensions (1 mg mL^{-1}). Irradiation was performed for 10 min using the light source previously described. Three distinct experimental conditions were employed to detect specific reactive species: (i) hydroxyl radicals were probed using 25 mM DMPO (purified with activated charcoal) in water; (ii) singlet oxygen was detected using 25 mM TEMP in water; and (iii) hole formation was assessed using 100 μM TEMPO in water. Control samples lacking photocatalyst were prepared in parallel under identical conditions. Following irradiation, 30 μL aliquots were transferred into 1 mm inner diameter glass capillaries, flame-sealed, and immediately analyzed by EPR spectroscopy.

2.3. Photocatalytic activity evaluation and scavenger experiments

Photocatalytic experiments were performed in a 250 mL jacketed beaker with a 50 W LED panel positioned above it. Temperature was controlled using water circulation, and the light intensity at 10 cm from the solution surface was 111 μW cm^{-2}. Further details on the reactor setup and lamp spectrum are provided in our earlier study (Ahmadi et al., 2024b). The schematics of the photocatalytic reactor are provided in Fig. S1. Air was supplied through a flow meter, and each experiment used 200 mL of solution. Before irradiation, samples were kept in the dark for 30 min to reach equilibrium. The reaction proceeded for 180 min, during which 2 mL samples were taken at intervals and filtered through a 0.45 μm PTFE syringe filter. A UV-Vis spectrophotometer (UV-2600, SHIMADZU) was used to measure paracetamol at 243 nm and to observe changes in the wastewater spectrum during treatment. The initial and final TOC values were obtained using a TOC analyzer (TOC-L, SHIMADZU). Ammonium oxalate (AO), furfuryl alcohol (FFA), isopropyl alcohol (IPA), and 1,4-Benzoquinone (BQ) were employed to scavenge h^+, ($^1O_2$), •OH, and O_2•$^-$ species, respectively. A 0.1 mM amount of the scavenger species was used in the experiments. The concentrations of scavengers were selected according to their solubility constraints and UV-Vis spectrophotometer limitations. All the photocatalytic experiments were repeated three times to ensure the reproducibility of the experiments.

To further evaluate the photocatalytic performance of the synthesized materials, the degradation kinetics of paracetamol were determined using a pseudo-first-order kinetic model, which is widely applied for photocatalytic degradation of organic pollutants. The kinetic model can be expressed as Equation (2), where C_0 and C_t represent the initial and time-dependent concentrations of paracetamol, respectively, and k is the apparent reaction rate constant (Wu et al., 2020, 2021; Wang et al., 2018).

$$\ln(C_0 / C_t) = kt \quad (2)$$

2.4. Selective photo-depositions of Pt and Mn

A solution containing 0.01 mmol of $H_2PtCl_6{\cdot}6H_2O$ or $Mn(acac)_2$ was added to 15 mL of ethyl acetate and sonicated for 5 min. Then, 50 mg of two-step 10% material (most effective photocatalyst in this study) was added to the solution and exposed to visible-light irradiation (50 W LED) at constant temperature (25 °C) using a jacketed beaker for 1 h. The resulting materials were collected by centrifugation, washed with absolute ethanol and MQ water, and finally dried at 60 °C overnight. Finally, EDX was carried out to see the deposition sites of Pt and Mn.

3. Results and discussion

3.1. Characterizations

Elemental quantification via XRF confirmed the presence of C, Ti, Bi, O, and Br in the sample, as shown in Table 1.

Nitrogen adsorption-desorption analyses were performed for glucose hydrochar, Bi_3O_4Br/TiO_2 NB, one-step, and two-step materials. The isotherms and the pore size distributions are presented in Figs. S2 and S3. Among the hydrochar containing samples, one-step 20% exhibits the largest specific surface area (Table 2). The specific surface area of one-step 10% and two-step 10% materials were determined to be 24 $m^2\ g^{-1}$ and 25 $m^2\ g^{-1}$, which are very close to each other.

The XRD diffractograms of Bi_3O_4Br, TiO_2 NB, and Bi_3O_4Br/TiO_2 NB are presented in Fig. S4 and discussed in detail in our previous works (Ahmadi et al., 2024b, 2025b). The XRD results of the one-step and two-step samples, presented in Fig. 1, show that the crystalline structure is almost similar to the Bi_3O_4Br/TiO_2 NB. The XRD diffractograms are very similar for two-step materials, including the intensities of the peaks. This shows that that the glucose hydrochar did not interfere with the formation of the crystalline phases of Bi_3O_4Br and TiO_2 NB during the two-step synthesis. Regarding one-step materials, as the amount of hydrochar increases the intensity of the peaks decreases, which indicates that the general crystallinity of the material is decreased because of the amorphous structure of the HC and the possible coverage of crystalline structures by amorphous carbon (Wu et al., 2020; Wang et al., 2018). While a certain degree of structural disorder may introduce additional active sites, excessive decrease in crystallinity can negatively affect charge transport by increasing the density of defect sites that act as recombination centers. In contrast, the two-step synthesis preserves the crystalline structure more effectively, which is beneficial for charge transport and overall photocatalytic performance. This interpretation is consistent with the photocatalytic results (Fig. 10), where the one-step samples exhibit lower degradation efficiency. In both one-step and two-step materials, no diffraction peak attributable to HC was observed due to its amorphous nature. Some peak shifts were observed with one-step and two-step materials (Fig. S5), of which the shifts for one-step materials were more significant. For example, the peak at around $2\theta = 34.42^\circ$ was negatively shifted to 34.1°, 34.18°, 34°, and 33.98° for 5% one-step, 10% one-step, 15% one-step, and 20% one-step, respectively. In addition, shifts from $2\theta = 34.42^\circ$ to 34.34°, 34.38°, 34.32°, and 34.26° for 5% two-step, 10% two-step, 15% two-step, and 20% two-step materials were noted, respectively.

To investigate the surface functional groups of the hydrochar (Fig. S6) and photocatalysts, DRIFT measurement was done (Maad et al., 2026). The broad absorption band observed around 3200-3560 cm^{-1} was attributed to O-H stretching vibrations, indicating the presence of hydroxyl groups from adsorbed water or surface hydroxyl functionalities. Aliphatic C-H stretching vibrations were identified near 2920-2985 cm^{-1}, corresponding to methylene and methyl groups. The bands at 1614 cm^{-1} were assigned to C=C stretching in aromatic or furan structures, while peaks around 1710 cm^{-1} indicated C=O vibrations from carbonyl groups. Additional features in the 968-1058 cm^{-1} range were attributed to C-O and C-O-C vibrations, suggesting the presence of ether and aliphatic oxygenated groups. The detection of bands near 1300-1454 cm^{-1} further confirmed vibrational modes associated with furan monomers, highlighting the formation of polyfuran structures. Overall, the FTIR spectra demonstrate that the hydrochar surface is rich in oxygenated functional groups, including hydroxyl, carbonyl, carboxyl, and ether moieties, which are likely to influence its interaction with reactive species and catalytic performance (Li et al., 2022; Dong et al., 2025; Yadav et al., 2024; Michel et al., 2024; Zhang et al., 2025b). The DRIFT results of the Bi_3O_4Br/TiO_2 NB, one-step, and two-step photocatalysts revealed the presence of various functional groups and characteristic vibrations (Fig. 2a and b). Broad bands observed around 3200-3650 cm^{-1} were assigned to O-H stretching vibrations of adsorbed water. This band looks similar between Bi_3O_4Br/TiO_2 NB and two-step materials, but with regards to one-step materials, as the amount of hydrochar increased, a small sharp band was observed at around 3484 cm^{-1}. Additionally, the band near 1616 cm^{-1}, associated with the O-H bending vibration of molecular water, became slightly more pronounced in the samples containing hydrochar (Imam et al., 2018, 2019). Weak aliphatic C-H stretching vibrations at around 2940 cm^{-1} were observed for all the materials. The Bi-Br stretching vibrations were detected at approximately 1394 cm^{-1}. This band became broader after the addition of hydrochar. Bi-O, Ti-O, and Ti-O-Ti vibrations appeared in the 450-980 cm^{-1} range, with the sharp Bi-O band around 848 cm^{-1} becoming less intense in samples with hydrochar content. The overlapping of several metal-oxygen vibrations in this region complicated precise assignments, but these features collectively confirmed the structural and compositional characteristics of the synthesized photocatalysts (Ahmadi et al., 2024b, 2025b).

The Raman spectrum of HC is presented in Fig. S7, showing the amorphous structure of the hydrochar. When the hydrochar was added to the Bi_3O_4Br/TiO_2 NB composite, a decrease in the intensity of Raman peaks was observed and more hydrochar led to significant intensity decline, which is consistent with the XRD results. Various noisy peaks related to hydrochar are present in one-step materials (Fig. 3a), which results in a wavy spectrum, while these peaks were not observed for the two-step materials (Fig. 3b). It is also observed that the peaks were

Table 2
BET results of the synthesized materials.

Sample	S_{BET} ($m^2.g^{-1}$)	Total pore volume ($cm^3.g^{-1}$)	Average Pore diameter (nm)
Glucose hydrochar	12	0.02	10
Bi_3O_4Br/TiO_2 NB	23	0.11	19
One-step 5 %	18	0.12	24
One-step 10 %	24	0.14	21
One-step 15 %	28	0.17	20
One-step 20 %	37	0.20	19
Two-step 5 %	21	0.13	27
Two-step 10 %	25	0.14	21
Two-step 15 %	24	0.14	22
Two-step 20 %	25	0.14	21

Table 1
XRF results of the synthesized materials.

Sample	Weight %					Atomic %					Compound %	
	Ti	Bi	O	Br	C	Ti	Bi	O	Br	C	TiO_2	Bi_3O_4Br
One-step 5 %	8.4	68.5	14.8	5.9	0.4	11.3	21.2	60.3	4.7	2.3	14	76.3
One-step 10 %	7.2	70.1	14.3	5.9	0.5	10.1	22.3	59.6	4.9	3.0	12	78.1
One-step 15 %	8.6	67.9	15.0	5.7	0.6	11.4	20.6	59.8	4.5	3.3	14.4	75.7
One-step 20 %	7.6	70.1	14.3	5.5	0.8	10.4	21.8	58.6	4.5	4.4	12.7	78.2
Two-step 5 %	7.1	61.3	12.5	7.8	0.2	11	21.9	58.4	7	1.2	12	75.4
Two-step 10 %	8.2	61.1	13.1	7.8	0.2	12.21	20.8	58.8	6.9	1.2	13.7	75.2
Two-step 15 %	9.1	65.4	14.2	8.3	0.3	12.5	20.6	58.4	6.8	1.6	15.3	80.4
Two-step 20 %	8.9	59.1	13.2	7.5	0.3	13.1	20	58.4	6.6	1.7	14.8	72.7

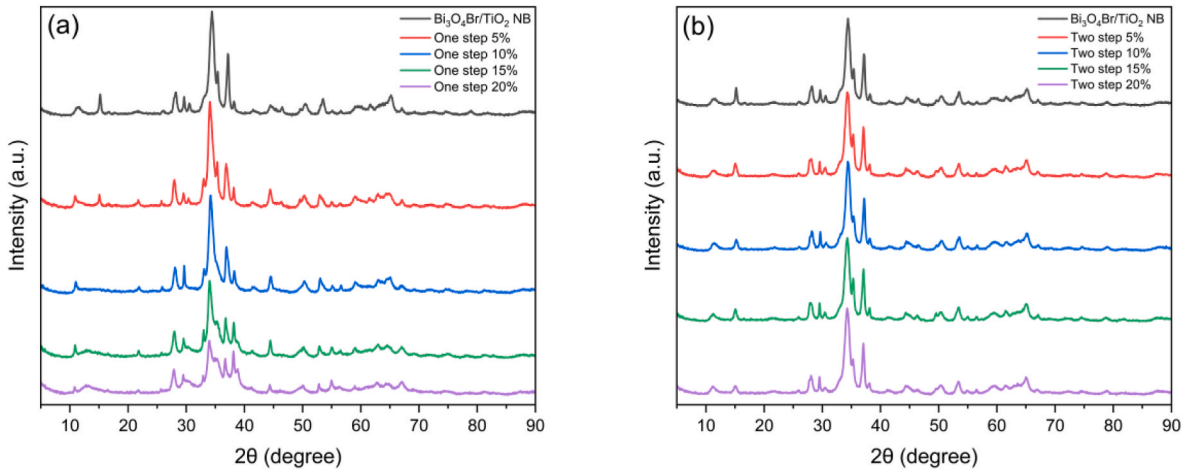

Fig. 1. XRD diffractograms of (a) one-step and (b) two-step photocatalysts.

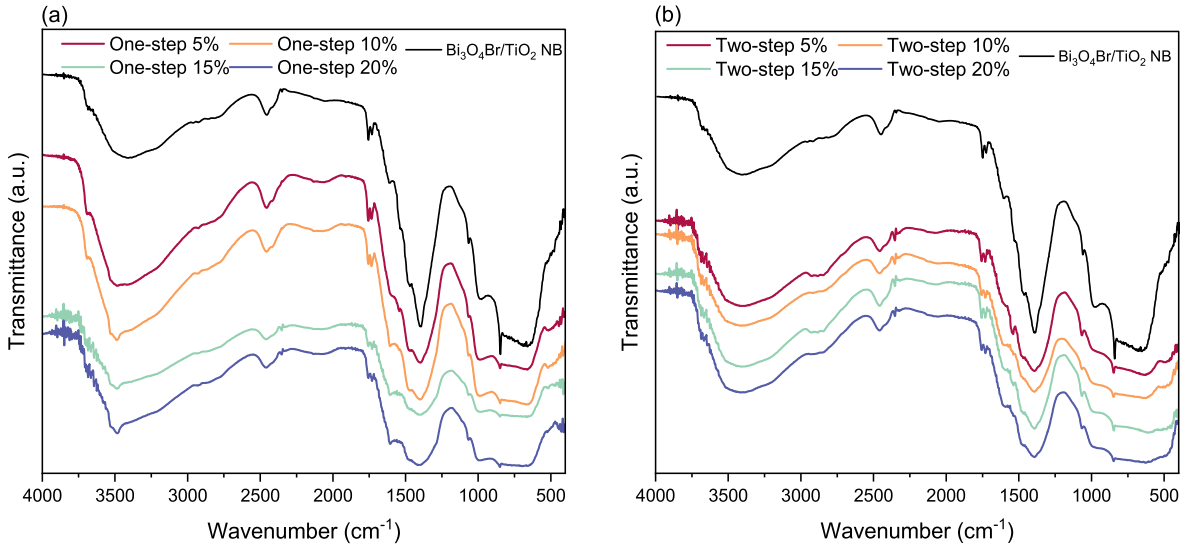

Fig. 2. DRIFT results of (a) one-step and (b) two-step materials.

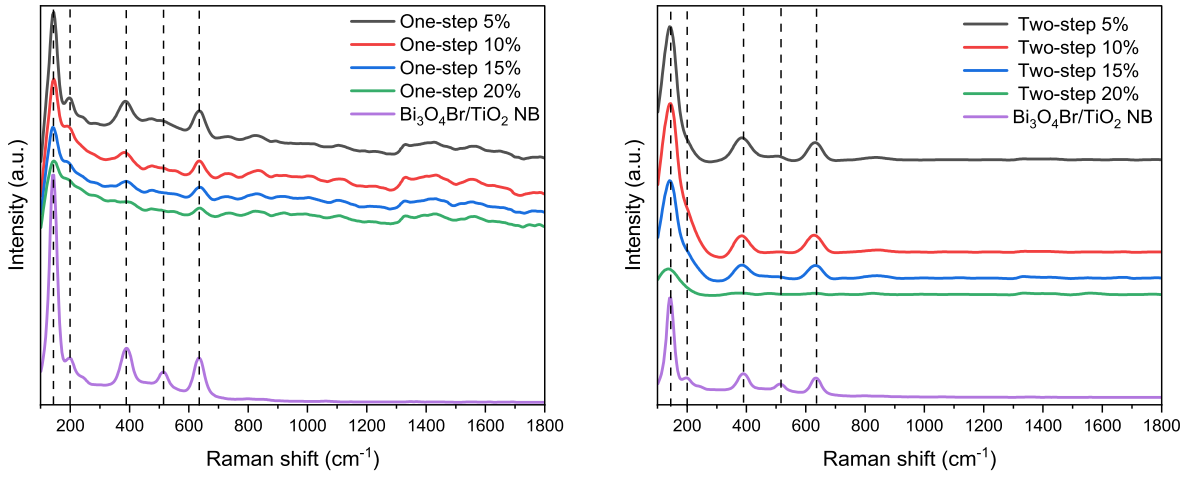

Fig. 3. Raman results of (a) one-step and (b) two-step materials.

broadened and negatively shifted after the addition of hydrochar for both one-step and two-step materials, leading to a decrease in crystallinity. This shift may result from interactions between Bi_3O_4Br/TiO_2 NB and the hydrochar surface (Sánchez-Silva et al., 2024).

Regarding Bi_3O_4Br/TiO_2 NB, there exist some peaks centered at 144, 199, 388, 514, and 635 cm^{-1}. All the peaks observed a tiny negative shift or remained at the same position after the addition of hydrochar. The peak observed at 144 cm^{-1} can be ascribed to E_{g1} (O-Ti-O symmetric bending) or E_g (internal Bi-Br stretching) modes due to overlapping of Bi_3O_4Br and TiO_2 NB Raman peaks. In our previous studies (Ahmadi et al., 2024b, 2025b), the B_{1g} modes of oxygen atom vibration were observed at around 376 cm^{-1}, while the peak observed at 399 cm^{-1} (B_{1g} mode), corresponds to O-Ti-O counter-bending and symmetric vibrations. Therefore, for the hydrochar containing materials, the peak at 388 cm^{-1} could be attributed to these. In addition, A_{1g} + B_{1g} mode corresponds to O-Ti-O counter-bending and symmetric vibrations appeared at 514 cm^{-1}.

X-ray photoelectron spectroscopy was conducted to investigate the surface chemical states of the synthesized materials. The survey spectra confirmed the presence of Ti, Bi, Br, O, and C in all hydrochar containing materials (Fig. S8). As expected, the hydrochar containing materials exhibited enhanced C 1s peak intensity compared to pristine Bi_3O_4Br/TiO_2 NB, verifying the coupling of hydrochar with the Bi_3O_4Br/TiO_2 NB. All binding energy values were calibrated using the adventitious carbon C 1s peak at 284.8 eV. The Ti $2p_{3/2}$ and Ti $2p_{1/2}$ peaks of Bi_3O_4Br/TiO_2 NB were positioned at 458.36 and 464.62 eV, characteristic of Ti^{4+} species. In hydrochar containing composites, both peaks displayed a slight negative shift of ~0.2 eV relative to Bi_3O_4Br/TiO_2 NB, implying strong coupling between Bi_3O_4Br/TiO_2 NB and hydrochar (Zhang et al., 2024; Cheng et al., 2019; Feng et al., 2023). Also, low-valent state of Ti species (Ti^{3+}) might exist in TiO_2 NB or some defects might have been formed by the reduction of Ti^{4+} during the hydrothermal synthesis of TiO_2 nanobelts as previously described in our earlier study (Fig. 4a and b) (Ahmadi et al., 2025b; Cheng et al., 2019). The high-resolution Bi 4f spectrum of Bi_3O_4Br/TiO_2 NB displayed characteristic Bi^{3+} peaks at 159.06 eV (Bi $4f_{7/2}$) and 164.36 eV (Bi $4f_{5/2}$) (Zhao et al., 2016). Upon introduction of hydrochar, both peaks shifted towards lower binding energies. This negative shift indicates a strong electronic interaction between hydrochar and Bi_3O_4Br/TiO_2 NB. It is consistent with the presence of unpaired electrons in the carbon atoms, which can strongly interact with the surface electrons of the Bi_3O_4Br/TiO_2 NB, thereby facilitating charge transfer transitions. This highlights the role of hydrochar in promoting interfacial charge transfer (Fig. 4c and d) (Yang et al., 2023). Similarly, the Br 3d spectrum of Bi_3O_4Br/TiO_2 NB featured $3d_{5/2}$ and $3d_{3/2}$ peaks at 68.38 and 69.44 eV, respectively. In the hydrochar containing materials, these peaks shifted slightly, confirming that Br^- anions also experience a modified electronic environment due to interfacial interactions (Fig. 4e and f) (Ju et al., 2025). Such shifts were observed by another study in lignin-biochar/BiOBr that further suggests facilitated charge transfer across the interface (Yang et al.,

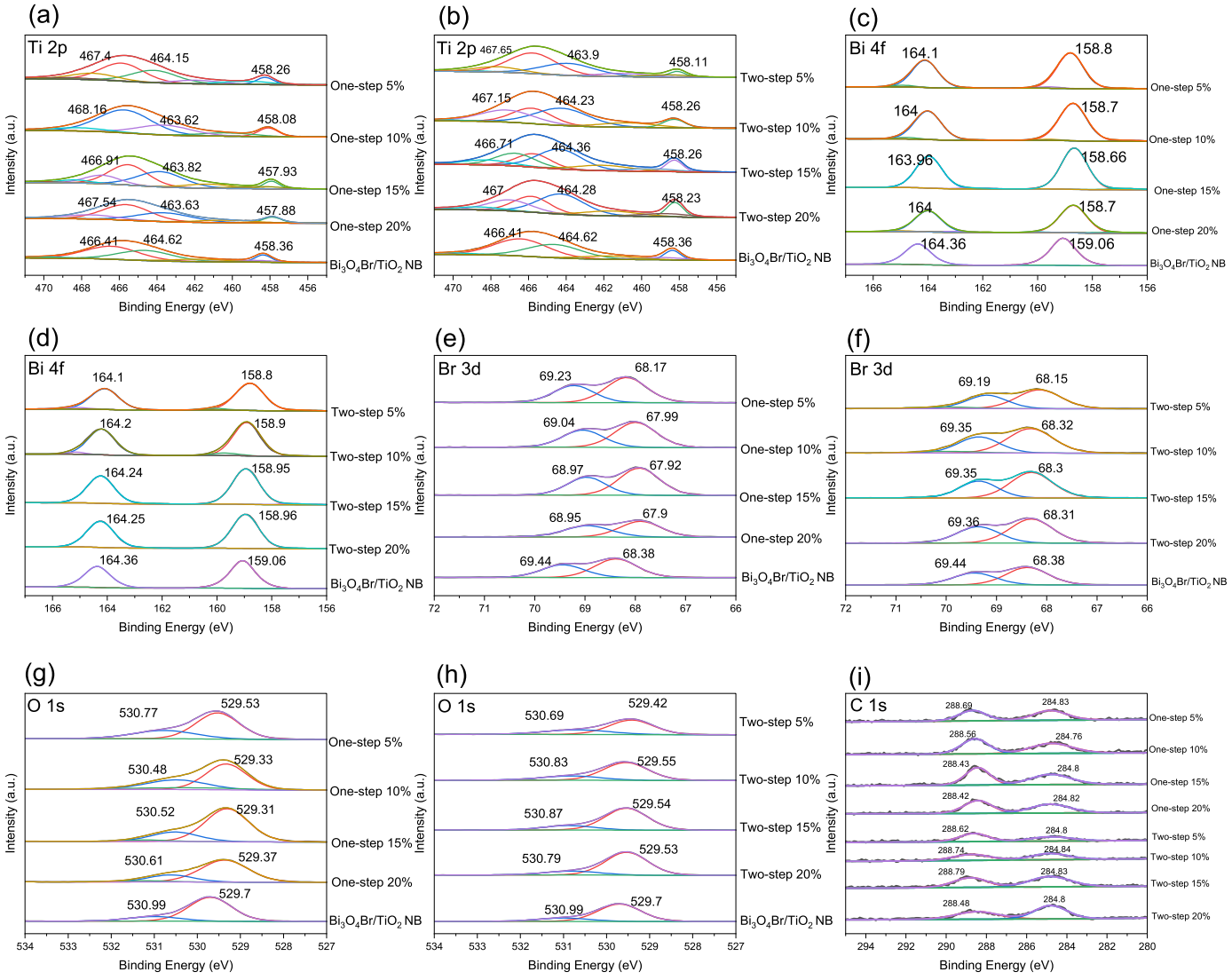

Fig. 4. High resolution XPS spectra of the synthesized materials.

2023). The O 1s spectra of Bi_3O_4Br/TiO_2 NB and hydrochar containing samples could be deconvoluted into two primary components centered at 529.70 eV and 530.99 eV, originating from lattice oxygen (Ti-O/Bi-O) and surface hydroxyl groups (-OH), respectively (Zhang et al., 2024; Wang et al., 2023). The O 1s peak shifted towards lower binding energies for all hydrochar containing materials compared to Bi_3O_4Br/TiO_2 NB (Fig. 4g and h). The C 1s spectra shows two peaks at 284.8 and 288.6-288.8 eV that were observed in all hydrochar containing samples. The former might correspond to C=C/C-C bonds, while the latter may be associated with oxygen-containing carbon species (C=O) (Fig. 4i) (Li et al., 2022). Overall, the negative shifts observed in the Bi 4f, Br 3d, Ti 2p, and O 1s binding energies of the hydrochar-containing samples clearly demonstrate strong interfacial electronic coupling between the hydrochar and the Bi_3O_4Br/TiO_2 NB.

The effect of hydrochar on the visible light absorption and bandgap of the composites was investigated. The UV-Vis DRS spectra in Fig. 5a reveals that all photocatalysts show a sharp absorption edge around 400 nm, but the intensity of absorption in the visible range (450-800 nm) increases markedly upon the addition of hydrochar (Fig. S9). Although the absorption edge of the one-step and two-step materials shifts slightly toward shorter wavelengths, the overall absorbance at longer wavelengths is noticeably enhanced compared with the Bi_3O_4Br/TiO_2 NB. This increase in visible-light absorption is attributed to the broad and continuous light-harvesting capability of the hydrochar, as well as to possible interfacial interactions between the semiconductor and the carbonaceous component. These effects enable the Bi_3O_4Br/TiO_2 NB to capture more visible photons despite the negative minor absorption edge shift, suggesting that hydrochar could improve the optical response of the materials. The same results were obtained by other studies (Dong et al., 2025; Qi et al., 2023; Zhang et al., 2025b; Fan et al., 2023; Liu et al., 2017). The bandgap of Bi_3O_4Br/TiO_2 NB was earlier determined to be 2.88 eV based on Kubelka-Munk equation (Ahmadi et al., 2025b; Makuła et al., 2018). The calculated bandgaps of the one-step and two-step materials are presented in Fig. 5b. Also, the bandgap energy diagram with more zooming and intercepts are presented in Fig. S10.

Glucose hydrochar has spherical morphology (Fig. 6a) with non-uniform carbon sphere sizes. Fig. 6b–i shows that the surface of the carbon sphere is covered by the Bi_3O_4Br/TiO_2 NB. The amount of carbon in the one-step and two-step materials is very low based on the XRF, and this is the reason why there are small amounts of spheres in the FESEM images. Figures with higher magnifications (20 KX and 50 KX) are presented in the supplementary materials (Figs. S11–S13). EDX results (Fig. 7a–b) show the uniform distribution of bismuth and titanium on the materials.

The presence of Bi_3O_4Br/TiO_2 NB heterojunction was earlier confirmed by TEM in our previous study (Ahmadi et al., 2025b). Comparing the TEM images of Bi_3O_4Br/TiO_2 NB (Ahmadi et al., 2025b), one-step 10% (Fig. 8a–b), and two-step 10% (Fig. 8c–d) materials, it can be inferred that there are some very dark spots in the TEM of these materials. Due to the very low amount of carbon, we cannot see the carbon sphere structures in the TEM images very well, but these dark places look like a round particle. Therefore, we can assume a carbon sphere covered by Bi_3O_4Br/TiO_2 NB is present there. In order to confirm whether these dark places are related to carbon spheres or not, the EDX has been carried out. The results shown in Fig. 8e–j confirmed the presence of carbon. The microstructure and interfacial characteristics of the synthesized two-step 10% photocatalyst were further investigated by HRTEM analysis, as shown in Fig. 9. HRTEM images reveal intimate contact between the TiO_2 nanobelts and Bi_3O_4Br, confirming successful heterostructure formation, with the Bi_3O_4Br phase attached to the TiO_2 nanobelt. Lattice fringes with interplanar distances of 0.282 nm and 0.374 nm correspond to the (020) plane of Bi_3O_4Br and the (201) plane of TiO_2 NB, respectively, and their well-resolved appearance confirms good crystallinity of both phases. A distinct interfacial region between the two components indicates strong coupling, which is favorable for efficient charge carrier migration and suppression of electron-hole recombination during photocatalysis.

3.2. Photocatalytic experiments

The degradation of paracetamol was investigated with the synthesized materials for 180 min (Fig. 10). The photolysis was determined to be 2% in our previous study (Ahmadi et al., 2025b). TiO_2 NB was able to degrade the paracetamol only 8% under visible light irradiation, while the degradation was calculated to be 58% for Bi_3O_4Br. There was an improvement in the degradation of paracetamol (76%) when the Bi_3O_4Br/TiO_2 NB heterojunction was employed. The photocatalysts, containing the glucose hydrochar, showed different behavior for the degradation of paracetamol. All the one-step materials experienced a decrease, whereas the two-step materials demonstrated an improvement in the degradation of paracetamol. In order to investigate the reason for this, PL and EIS were carried out (Fig. 11). One-step 10% and two-step 10% samples were selected for these measurements and the results supported the photocatalytic degradation experiments. Both PL and EIS indicated that the emission intensity of two-step 10% is the lowest, leading to the highest separation efficiency of photogenerated charge carriers. Also, it is observed that the emission intensity of one-step 10% is higher than Bi_3O_4Br/TiO_2 NB, which could support the photocatalytic degradation results. It should be noted that the EIS measurements were

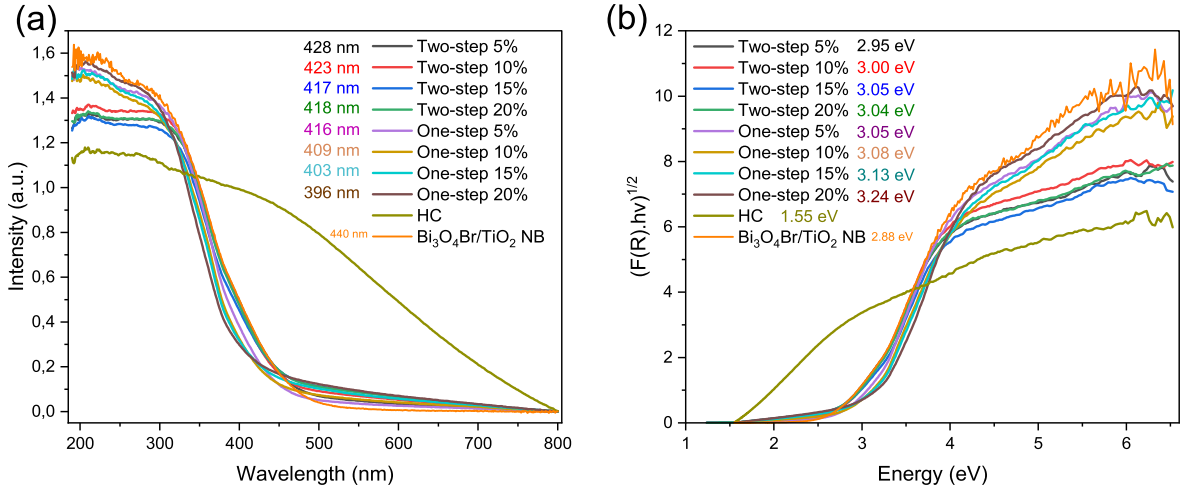

Fig. 5. (a) UV–Vis DRS and (b) band gap energies.

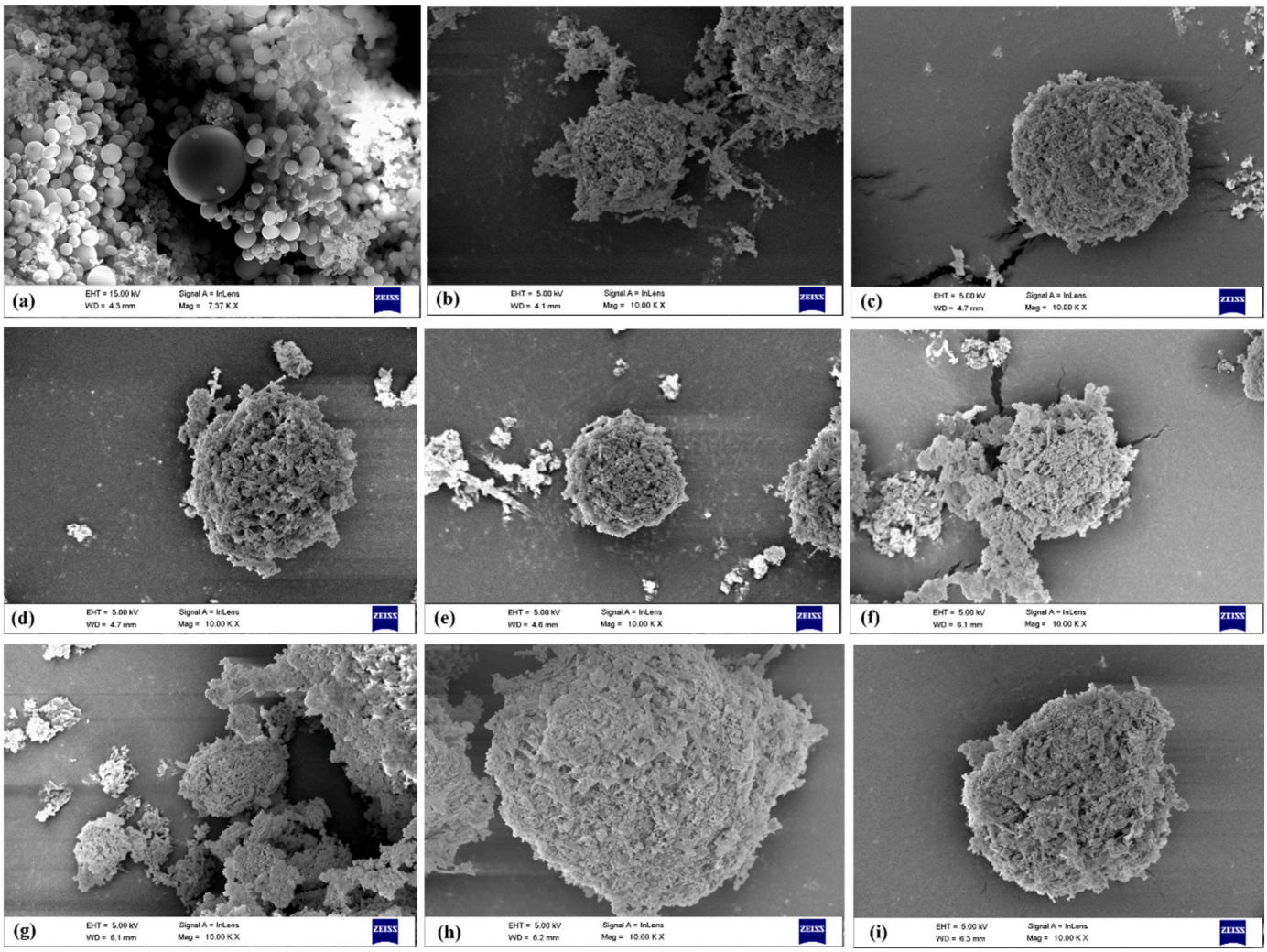

Fig. 6. FESEM images of (a) glucose hydrochar, (b) one-step 5%, (c) one-step 10%, (d) one-step 15%, (e) one-step 20%, (f) two-step 5%, (g) two-step 10%, (h) two-step 15%, and (i) two-step 20%.

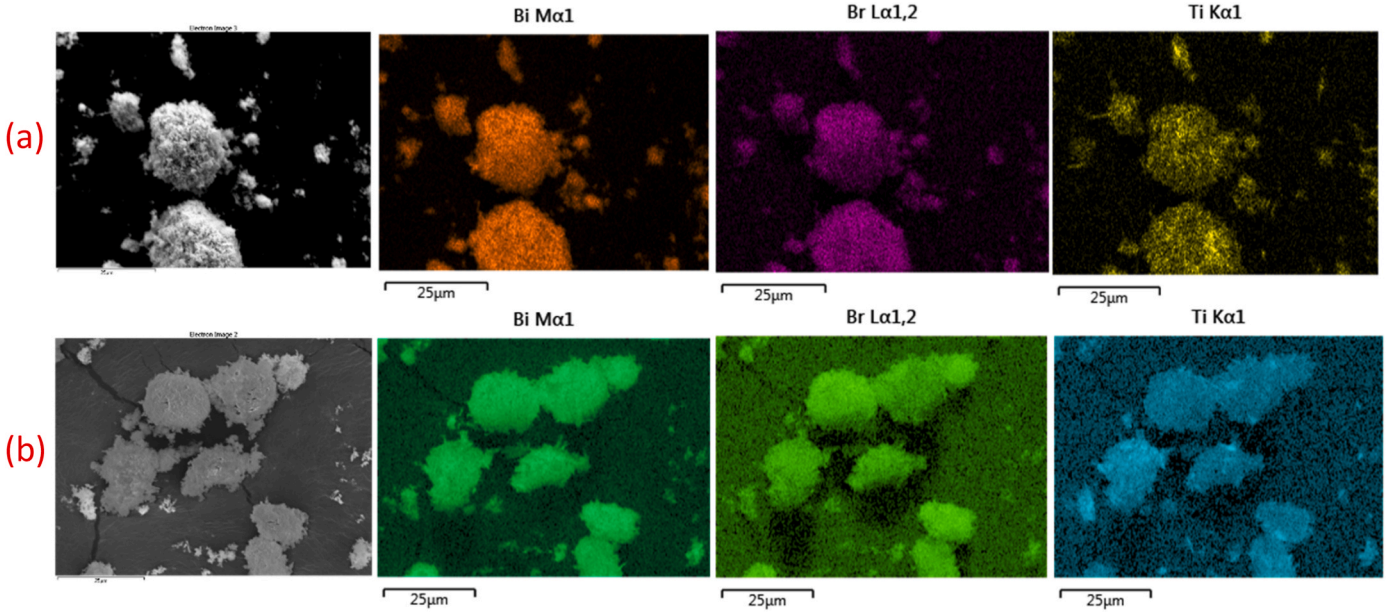

Fig. 7. EDX results of (a) one-step 10% and (b) two-step 10%.

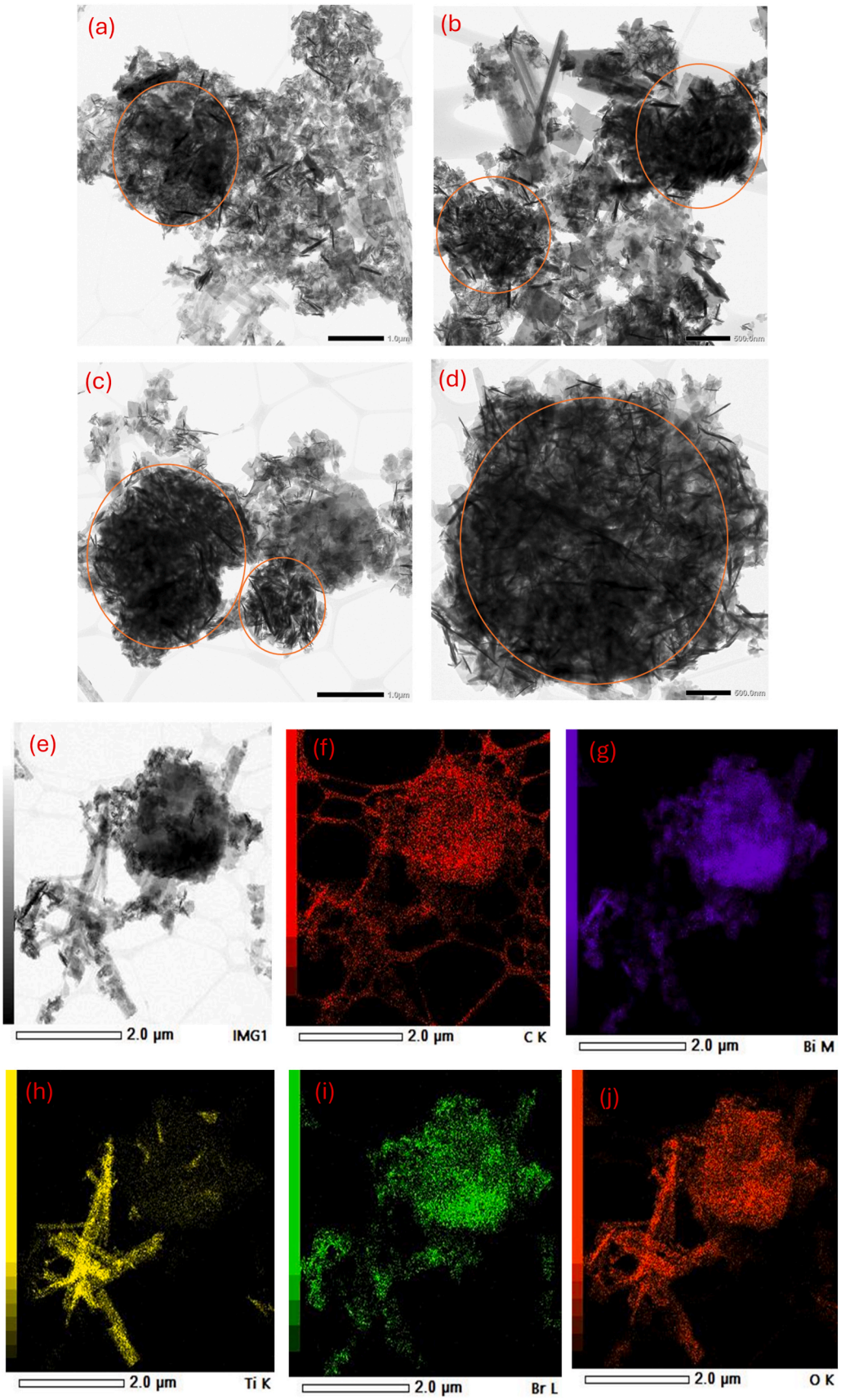

Fig. 8. TEM results of (a-b) one-step 10%, (c-d) two-step 10%, (e-j) EDX results of two-step 10%.

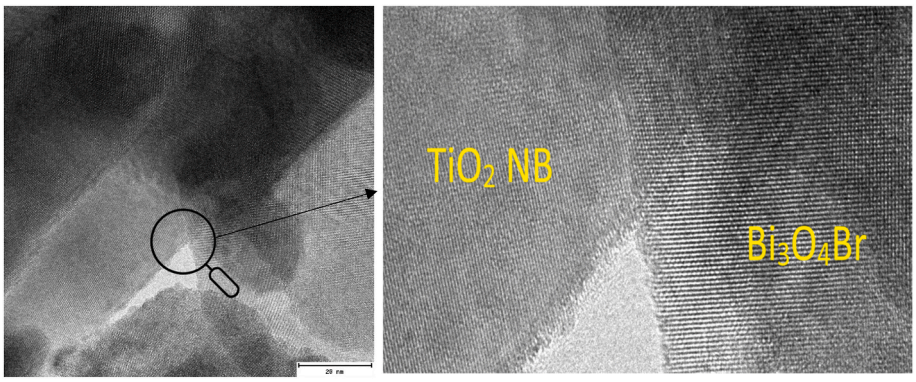

Fig. 9. HRTEM of two-step 10%.

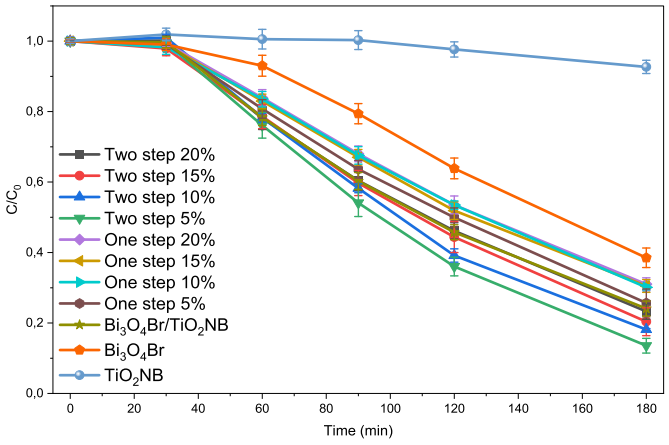

Fig. 10. Photocatalytic degradation of paracetamol under visible light irradiation.

performed on pressed powder pellets; therefore, the results primarily reflect bulk and contact resistance rather than direct interfacial charge transfer under photocatalytic conditions in solution. Nevertheless, the arc radius of two-step 10% sample is lower than that of Bi_3O_4Br/TiO_2 NB and one-step 10%, resulting in the best electron-hole separation. This trend is consistent with the PL results and enhanced photocatalytic performance, supporting more efficient charge separation. Therefore, the improved photocatalytic performance of two-step 10% was due to its higher carrier separation rate and lower charge transfer resistance.

As shown in Fig. 10, the degradation data exhibits a good linear relationship when plotted versus irradiation time, indicating that the photocatalytic degradation process follows pseudo-first-order kinetics. The corresponding linear fitting plots and calculated rate constants for all synthesized photocatalysts are presented in Fig. S14. The obtained rate constants clearly demonstrate that the two-step synthesized photocatalysts exhibit significantly higher reaction rates compared to the one-step counterparts, which is consistent with their superior photocatalytic performance. For example, the rate constant (k value) for two-step 10% and one-step 10% is 0.3063 min^{-1} and 0.02004 min^{-1}, respectively.

The effect of initial pH on paracetamol degradation (using two-step 10% photocatalyst) was evaluated at pH 4, 6.5 (natural without adjustment), and 10. As shown in Fig. 12a, degradation efficiency was lowest (76%) under acidic conditions (pH 4), likely due to TiO_2 agglomeration, which reduces surface area and light absorption. Compared to our previous study where only Bi_3O_4Br/TiO_2 NB was used, there is an improvement in the degradation of paracetamol under acidic conditions when HC is present in the heterojunction, showing that HC can contribute to activity or durability of the heterojunction under acidic conditions. Higher efficiencies were achieved at natural (pH 6.5, 87%) and alkaline pH (pH 10, 82%) after 180 min. Therefore, neutral pH offers optimal conditions, ensuring high degradation efficiency. In addition, the solution pH had an effect on the degradation kinetics. The rate constant (k value) increased from 0.02556 min^{-1} at pH = 4 to a maximum value of 0.0327 min^{-1} at pH = 11 (Fig. S15 and Fig. S16).

The impact of different concentrations of paracetamol is shown in Fig. 12b. The degradation efficiency of 5, 10, 15, and 20 mg L^{-1} was determined to be 92%, 87%, 80%, and 54%, respectively. The degradation efficiency was gradually decreased by increasing of paracetamol concentration until a significant decline was observed with 20 mg L^{-1} of

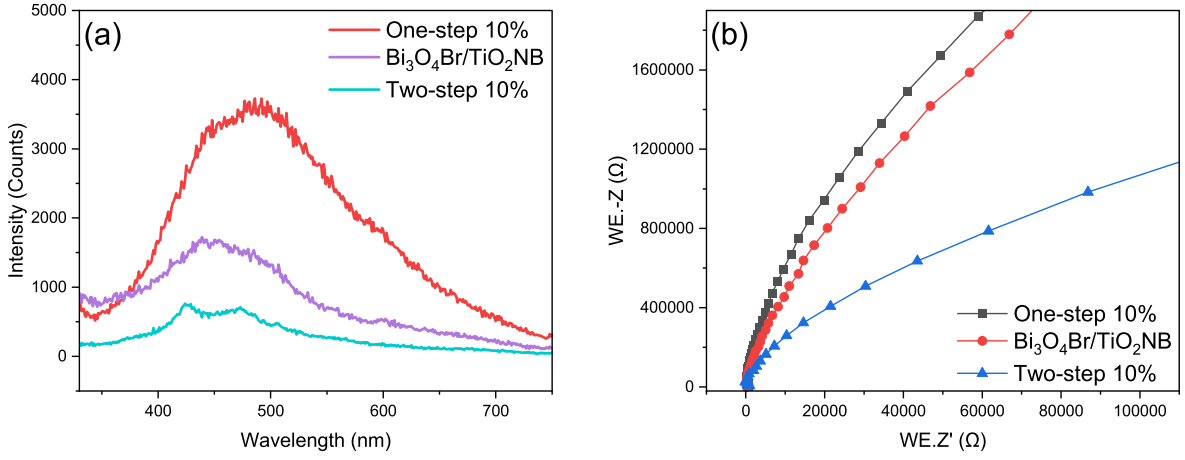

Fig. 11. (a) PL spectra and (b) EIS results.

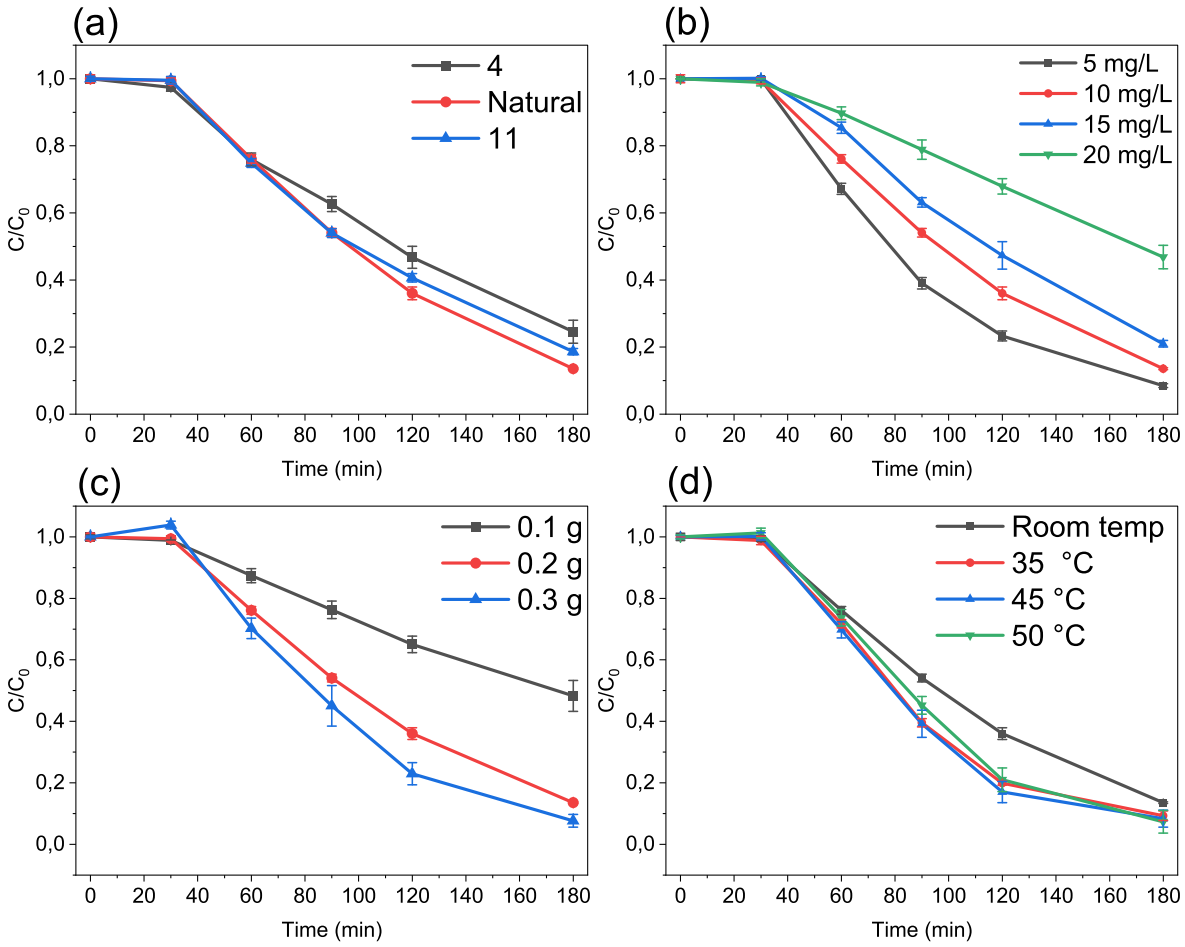

Fig. 12. The effect of (a) pH, (b) pollutant concentration, (c) photocatalyst dosage, and (d) temperature on the degradation of paracetamol.

paracetamol. This behavior is consistent with previous works (Niu et al., 2026; Abdul-Raheem et al., 2025), where reduced degradation efficiency at increased pollutant's concentrations was observed. The initial paracetamol concentration significantly influenced the reaction rate. The highest rate constant (0.07554 min^{-1}) was observed at an initial concentration of 5 mg L^{-1}, while further increases in concentration led to a gradual decrease in rate constant (Fig. S15 and Fig. S16). To evaluate the influence of photocatalyst dosage on paracetamol degradation, photocatalyst masses of 0.1, 0.2, and 0.3 g were used while maintaining the other parameters constant. As illustrated in Fig. 12c, the degradation efficiency increased steadily with higher photocatalyst loading, reaching 52%, 87%, and 93% for 0.1 g, 0.2 g, and 0.3 g of the two-step 10% photocatalyst, respectively. This improvement is mainly due to greater production of reactive species and availability of active sites at higher photocatalyst dosages, which can contribute to good catalytic performance.

The influence of temperature on paracetamol degradation was examined, and the experiments were performed at room temperature (23 °C), 35 °C, 45 °C, and 50 °C for 180 min. As shown in Fig. 12d, the raising of the temperature increased paracetamol degradation. The degradation performance at 35 °C (91%), 45 °C (92%), and 50 °C (93%) after 180 min is quite close to each other. In general, the improvement of the paracetamol degradation after temperature rise could be attributed to promoting greater production of hydroxyl radicals at higher temperatures, thereby accelerating the photocatalytic degradation process (Ahmadi et al., 2025b; Janus et al., 2012; Hosny et al., 2022). Kinetic studies revealed that the reaction kinetics improved with increasing temperature, with the rate constant rising from 0.3063 min^{-1} at room temperature to 0.04399 min^{-1} at 50 °C (Fig. S15 and Fig. S16).

Table 3 compares the experimental conditions and degradation efficiencies obtained in this study with those reported in previous investigations. In overall, it is challenging to compare different studies due to differences in reactors and experimental conditions that impact the reaction. In our study, we used 50W LED panel (the spectrum can be found in our previous study (Ahmadi et al., 2024b)) as a light source, which is more sustainable than UV lamps or the power consumption is much lower than in the studies mentioned in the table.

It should be noted that the TOC removal of paracetamol was evaluated to be 63% with 0.2 g of two-step 10% photocatalyst. The experiment was done at a natural pH of paracetamol and room temperature, using 10 mg L^{-1} of paracetamol without any scavengers.

3.3. Studies on the mechanism of degradation

To suppress specific reactive species in the photocatalytic degradation of paracetamol, ammonium oxalate (AO) targeted h^+, furfuryl alcohol (FFA) scavenged singlet oxygen, isopropyl alcohol (IPA) quenched •OH radicals, and benzoquinone (BQ) scavenged $O_2^{\bullet-}$. The results (Fig. 13a) indicated that holes have the primary contribution to the degradation of paracetamol as the degradation efficiency decreased from 93% to 37% (≈60% percentage point decrease). At the catalyst surface, photogenerated holes can act as reactive oxidizing species that have the potential to directly target and break down pollutant molecules. The extent of degradation depends on how effectively the pollutants interact with and adsorb onto the photocatalyst (Li et al., 2024). In addition, highly reactive hydroxyl radicals are produced as a result of the interaction of holes with surface -OH groups or adsorbed water molecules (Li et al., 2024). The degradation efficiency was also reduced

Table 3
Comparison of our study with other existing studies.

Photocatalyst	Process parameters						Degradation efficiency (%)	Reference
	pH	Dosage (g L^{-1})	Initial concentration (mg L^{-1})	Reaction time (min)	Light source	Temperature (°C)		
TiO_2/Nb_2O_5	-	0.6	30	-	40 W LED	-	90.6	Bi et al. (2021)
La-doped ZnO	-	1	100	180	3*20 W fluorescent lamps	25	99	Thi and Lee (2017)
Bi_2O_3/MnO_2	6.8	1	5	300	200 W LED	27	94.3	Parida et al. (2023)
Ag/ZnO	11	0.75	5	35	8 W UV	-	94	Mohsentabar et al. (2023)
$Cu_2O/WO_3/TiO_2$	9	0.25	1	60	150 W xenon lamp	room temperature	92.5	Chau et al. (2022)
Fe-TiO_2	3.5	-	25	215	7*36 W UVA	-	96.6	Puri et al. (2021)
ZnO/g-C_3N_4	9	0.2	30	60	500 W xenon lamp	-	95	Hassan et al. (2024)
(P, S)-doped g-C_3N_4/TiO_2	7	1	20	60	xenon lamp	20	99.5	Cako et al. (2023)
Fe_3O_4/BiOBr@HC	6	0.6	10	40	50 W LED	Room temperature	100	Li et al. (2022)
TiO_2/hydrochar	3.6	0.5	50	70	250 W xenon lamp	Ambient	100	Zhang et al. (2024)
Ag/AgBr/Bi_2WO_6/CHC	7	1	10	90	50 W LED	-	97.5	Dong et al. (2025)
Bi_2WO_6/TiO_2/HC	6	1	10	60	50 W LED	-	99.5	Qi et al. (2023)
Bi_3O_4Br/TiO_2 NB/GH	6.5	0.2	10	180	50 W LED	35	91	This study

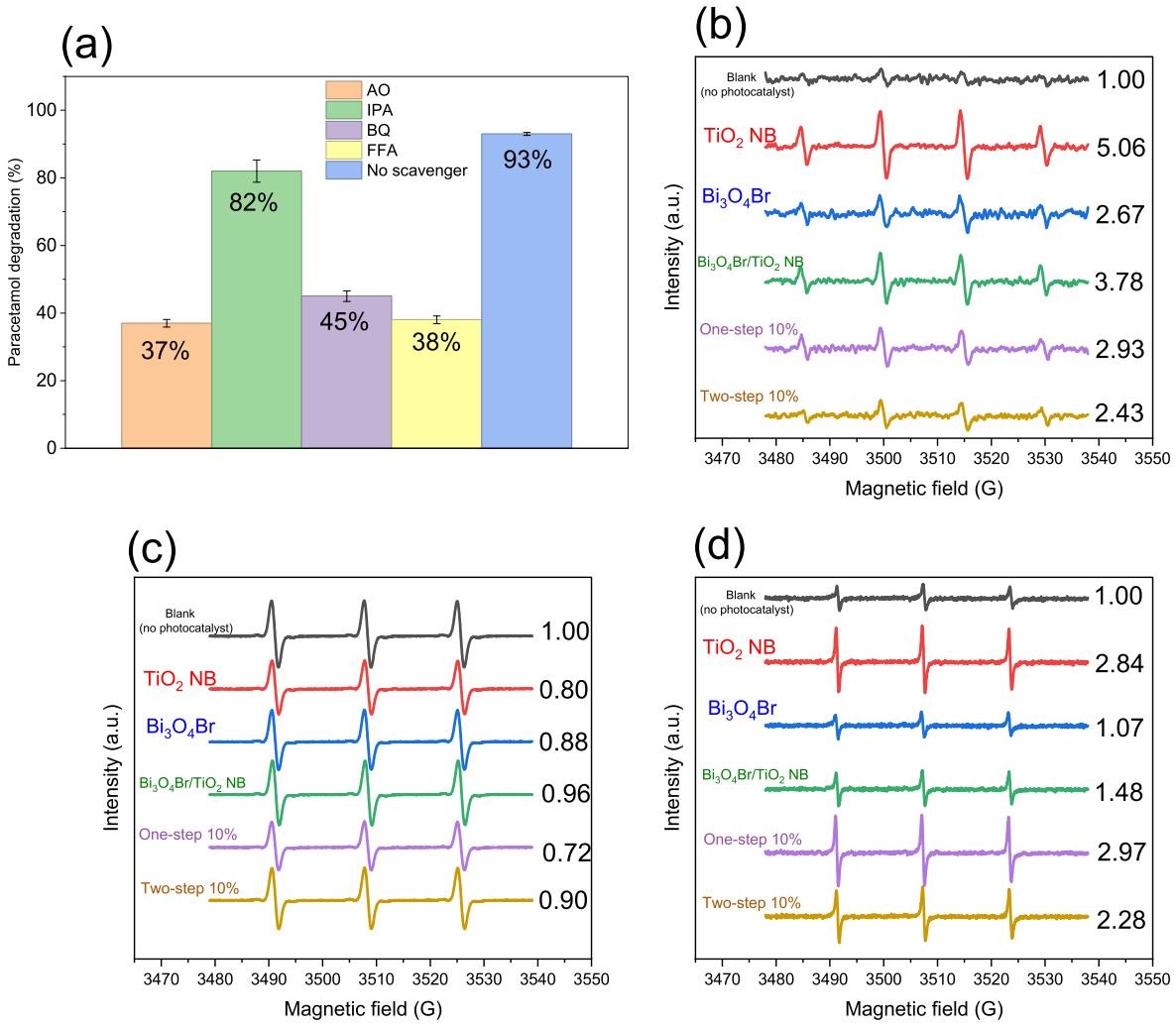

Fig. 13. (a) Scavenger experiments with two-step 10%, (b) EPR spectrum of hydroxyl radicals, (c) EPR spectrum of hole radicals, and (d) EPR spectrum of singlet oxygen.

to 38% and 45% in the presence of FFA (≈55% percentage point decrease) and BQ (≈48% percentage point decrease), showing that the

singlet oxygen and superoxide radicals contribute largely to the photocatalytic degradation of paracetamol as well. The addition of IPA decreased efficiency slightly to 82%, indicating the role of hydroxyl radicals in our system (≈11% percentage point decrease).

To compare the generation of reactive species by the synthesized photocatalysts under visible light irradiation, hydroxyl radical production was monitored using DMPO (Fig. 13b). Irradiation of DMPO in water alone led to the formation of the DMPO-•OH adduct via water radiolysis; this signal was adopted as the reference (intensity = 1.00). All photocatalysts produced hydroxyl radicals, with TiO_2 NB exhibiting the highest relative intensity (5.06). Hole (h^+) formation was investigated using the spin label TEMPO, which loses its EPR signal upon oxidation to $TEMPO^+$ after donating its unpaired electron to h^+. Fig. 13c shows the spectra of 100 μM TEMPO in aqueous solution after irradiation, both in the absence and presence of photocatalysts. No change in signal intensity was observed without photocatalyst (intensity = 1.00). The greatest signal decay occurred with the one-step 10% photocatalyst, reducing the TEMPO signal to 72% of its initial intensity. Given the initial TEMPO concentration of 100 μmol L^{-1}, this corresponds to the detection of 28 μmol L^{-1} of holes generated under the experimental conditions. Singlet oxygen formation was assessed using TEMP in aqueous suspensions, where its reaction with singlet oxygen ($^1O_2$) generates the stable radical TEMPO, detectable by EPR (Fig. 13d). A weak TEMPO signal was observed as a background spectrum, likely due to minor impurities in the TEMP sample, and remained unchanged during 10 min of irradiation in the absence of photocatalyst. This baseline signal was used as the reference (intensity = 1.00). The strongest $^1O_2$ signals were observed for the one-step 10% material and TiO_2 NB, with relative intensities of 2.97 and 2.84, respectively. Photocatalytic degradation studies have traditionally focused on the hydroxyl radical (•OH) as one of the major reactive oxygen species (ROS) involved in pollutant degradation. However, recent reports suggest that the role of singlet oxygen ($^1O_2$) should also be considered (Kuk et al., 2023). Moreover, $^1O_2$ has been proposed as an alternative oxidative pathway for selective oxidation of target compounds in complex matrices (Chen et al., 2021; Xu et al., 2022). Importantly, the formation of $^1O_2$ is believed to involve superoxide ($•O_2^-$) as a key intermediate, suggesting a mechanistic link between different ROS species (Xu et al., 2022). The detection of holes (h^+) using TEMPO further complements our results, as hole-mediated oxidation is a critical step in initiating ROS formation. The one-step 10% photocatalyst, for instance, exhibited the highest hole generation capacity, which correlated with elevated levels of both $^1O_2$ and •OH.

3.4. Reusability and performance of the two-step 10% material towards real wastewater treatment

The decrease in photocatalytic activity observed after repeated cycles can be attributed to the accumulation of intermediate products on the catalyst surface and partial blockage of active sites. Such behavior is commonly reported in photocatalytic systems and represents a key challenge for practical implementation. Despite this decline, the photocatalyst maintains a considerable level of activity after multiple cycles, indicating its potential for further optimization through improved regeneration strategies or catalyst immobilization approaches.

Reusability is a key consideration for the practical use of photocatalysts. To obtain initial information about stability, the two-step 10% photocatalyst was tested over five degradation cycles. As shown in Fig. 14, the paracetamol degradation efficiency remained at 64% after the fifth cycle. The decline in performance may be attributed to the formation of intermediate products in the pores and on active sites. Such behavior is commonly reported in photocatalytic systems and represents a key challenge for practical implementation. Despite this decline, the photocatalyst maintains a considerable level of activity after multiple cycles, indicating its potential for further optimization through improved regeneration strategies or catalyst immobilization approaches.

The two-step 10% was also used in degrading real diluted pharmaceutical wastewater over 24 h at dosages of 0.2 g and 0.4 g. The pH of real wastewater was measured to be 11.1. It should be noted that the 1% and 5% diluted wastewater had a pH of 9.8 and 10.2, respectively. As indicated in Table 4, TOC removal of 5% diluted pharmaceutical wastewater improved when the photocatalyst amount increased from 0.2 g (23%) to 0.4 g (32%). However, TOC removal remained almost

Table 4
TOC removal results of real pharmaceutical wastewater.

Pollutant	Photocatalyst dosage (g)	Time (h)	Initial TOC (mg L^{-1})	Final TOC (mg L^{-1})
1% real pharmaceutical wastewater	0.2	24	89.2	62.1
5% real pharmaceutical wastewater	0.2	24	448.1	345.5
1% real pharmaceutical wastewater	0.4	24	89.2	62.2
5% real pharmaceutical wastewater	0.4	24	448.1	305.3

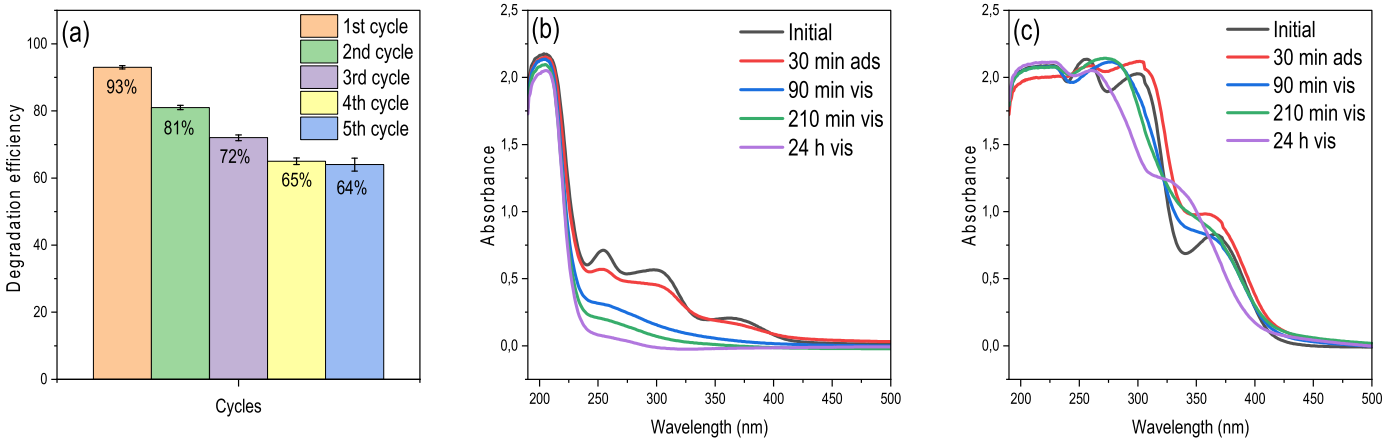

Fig. 14. (a) Reusability studies, UV–Vis spectra of (b) 1% diluted real pharmaceutical wastewater degradation in 24 h and (c) 5% diluted real pharmaceutical wastewater degradation in 24 h.

constant for both 0.2 g (30%) and 0.4 g (30%) of photocatalyst for the degradation of 1% diluted pharmaceutical wastewater. Fig. 14b–c displays the UV-Vis spectra of real pharmaceutical wastewater at different percentages of dilution (1% and 5%).

The morphology of the photocatalyst after degradation of paracetamol was investigated by FESEM images (Fig. 15a and b for the fresh and Figs. 15c and d for the recovered). Based on the images the recovered photocatalyst (two-step 10%) indicates good structural stability. The Bi_3O_4Br nanoflakes and TiO_2 nanobelts can be clearly observed both at low and high magnifications. TEM imaging supported further the FESEM results. The Bi_3O_4Br nanoflakes, TiO_2 nanobelts, and glucose hydrochar can be observed in Fig. 15e (fresh) and Fig. 15f (recovered). EDX analysis also confirmed a similar distribution of elements for fresh and recovered samples (Fig. S17). To gain more information about the stability of photocatalysts, FTIR and XRD analyses were performed. XRD patterns of the fresh and recovered catalysts (Fig. 15g) exhibit sharp diffraction peaks corresponding to the crystalline phases of Bi_3O_4Br and TiO_2 NB. No peak shifts were observed for the used catalyst, indicating structural and phase stability. FTIR results (Fig. 15h) showed that the broad absorption bands around 3500 cm^{-1}, assigned to the O-H stretching vibrations of surface hydroxyl groups and adsorbed water molecules, were observed for both the fresh and the recovered samples. The bands, which were assigned to metal-oxygen bonds at lower wavenumber region, supported the existence of Bi-O and Ti-O. However, the recovered photocatalyst showed a new small absorption band around 1160 cm^{-1}, which is attributed to C-O stretching vibration. In addition, sharper aliphatic C-H bands for the recovered photocatalyst at 2854, 2925 and 2960 cm^{-1} can be assigned to adsorbed paracetamol degradation products and intermediate species, such as muconic acid and oxalic acid, although they were also present in fresh photocatalyst and partly be originated from the residual ethylene glycol used in the synthesis (Ahmadi et al., 2024b, 2025b). From the above-mentioned discussion, it can be inferred that the adsorbed paracetamol intermediate species could be one of the reasons for decline in the activity. The long-term stability and potential metal leaching of photocatalysts are critical parameters governing their practical applicability in water treatment systems. The release of metal ions into the treated solution not only compromises catalyst reusability but may also introduce secondary contamination, thereby undermining the remediation objective. To evaluate the stability of the two-step 10% photocatalyst, inductively coupled plasma mass spectrometry (ICP-MS) was employed to quantify the concentration of leached Bismuth (Bi) and Titanium (Ti) ions in the reaction solution after the 1st and 5th photocatalytic paracetamol degradation cycles. Titanium leaching remained negligible throughout the cycling experiments. The Ti concentration in solution increased marginally from 0.09 μg L^{-1} after the 1st cycle to 0.67 μg L^{-1} after the 5th cycle. Bi leaching exhibited a more pronounced and progressive trend across the five cycles. The Bi concentration rose from 8.57 μg L^{-1} after the 1st cycle to 149.00 μg L^{-1} after the 5th cycle, representing a 17-fold increase.

3.5. Charge transfer and reaction mechanism

Photo-deposition methods were employed to determine the location of electrons and holes, utilizing $H_2PtCl_6{\cdot}6H_2O$ and $Mn(acac)_2$ as precursors (Zhao et al., 2024; Guan et al., 2021). When light is irradiated, Pt nanoparticles preferentially develop at areas with electron accumulation, while MnO_x signifies zones abundant in photogenerated holes. As shown in Fig. 16a, Pt is mainly located on the Bi_3O_4Br. In comparison, MnO_x species are mainly detected on the TiO_2 NB (Fig. 16b). These findings offer compelling evidence for the creation of a Z-scheme heterojunction involving Bi_3O_4Br and TiO_2 NB as shown in Fig. 17. In this mechanism, photogenerated electrons are accumulated in Bi_3O_4Br, whereas holes are accumulated in TiO_2 NB.

Based on the analysis of the band structure and experimental findings, a plausible photocatalytic mechanism for the Bi_3O_4Br/TiO_2 NB/hydrochar system can be suggested. As shown schematically (Fig. 17), Bi_3O_4Br, TiO_2 NB, and hydrochar are excited by photons, producing electrons in the conduction bands (CB) and holes in their valence bands (VB). The CB and VB edge potentials of TiO_2 NB are positioned at −0.59 eV and 2.62 eV, respectively, whereas Bi_3O_4Br shows a more negative CB level (−0.83 eV) and a less positive VB level (1.90 eV). Electrons excited by light in the conduction band of TiO_2 NB often move towards hydrochar and then recombine with holes in the valence band of Bi_3O_4Br. In this process, hydrochar may serve as an efficient electron mediator because of its electrical conductivity and surface oxygen-containing functional groups (hydroxyl, carbonyl, and carboxyl), thus enhancing interfacial charge transport. The electrical conductivity of the glucose-derived hydrochar (Fig. S18) was measured under compression up to 2000 kg cm^{-2}. The conductivity ranged from 3.16×10^{-1} to 1.77×10^{-1} S cm^{-1}. This low conductivity is characteristic of hydrochars synthesized at low temperatures (160 °C to 180 °C) and reflects the predominantly amorphous carbon structure with abundant oxygen-containing functional groups (Ren et al., 2020). Although the bulk conductivity is low, this does not hinder photocatalytic performance, as photocatalytic reactions are primarily surface-driven processes. The presence of surface functional groups may promote interfacial charge transfer during photocatalytic degradation. The C=O group on the surface of hydrochar can function as electron acceptor and temporarily accept and shuttle electrons (Dung et al.; Zhang et al., 2023). Consequently, electrons with significant reduction potential are retained in the CB of Bi_3O_4Br, whereas highly oxidative holes exist in the VB of TiO_2 NB. The collected electrons in the conduction band of Bi_3O_4Br (−0.83 eV) have adequate reduction potential to catalyze dissolved oxygen and produce superoxide radicals ($\bullet O_2^-$). Simultaneously, the holes preserved in the VB of TiO_2 NB (2.62 eV) can oxidize water or hydroxide ions that are adsorbed on the surface to generate hydroxyl radicals (•OH), in addition to direct oxidation of molecules of organic pollutants (Li et al., 2024). Moreover, hydrochar can aid in improved light absorption, offer additional adsorption sites, which boost the pollutant-catalyst interaction and facilitate the generation of reactive oxygen species. The surface oxygen-containing functional groups play a crucial role in the ability of hydrochar to promote reactive oxygen species generation (Chen et al., 2025). As evidenced by the EPR results of our study, the hydrochar-containing samples exhibit a strengthened singlet oxygen signal and enhanced hole participation. The combined effects of effective charge separation, maintaining the favorable redox potential, and the electron-shuttling function of hydrochar enable the continuous generation of reactive species like $\bullet O_2^-$, •OH, and h^+, which engage in the sequential oxidation and mineralization of pollutants. This Z-scheme heterojunction design significantly improves photocatalytic efficiency by optimizing charge utilization and preserving robust oxidation-reduction ability in the Bi_3O4Br/TiO_2 NB/hydrochar composite. Similar results were obtained in the literature (Li et al., 2020, 2022; Niu et al., 2026; Abdul-Raheem et al., 2025; Zhou et al., 2023).

4. Conclusions

The Bi_3O_4Br/TiO_2 NB/GH ternary photocatalyst with excellent performance in the visible light-driven degradation of paracetamol was successfully synthesized. The comparison between one-step and two-step methods showed that the method is important to reach improved structure integrity, interfacial charge transfer, and overall photocatalytic activity. Compared with the one-step method, the two-step method allowed Bi_3O_4Br nanosheet growth with high density and interlocking on the TiO_2 NB/GH framework leading to high interfacial charge transfer, effective charge separation, and low electron-hole recombination rates, proven by PL and EIS analyses. The two-step 10% had the highest photocatalytic activity, with about 91% degradation efficiency of paracetamol at natural pH (6.5). The optimization studies revealed that increasing the initial paracetamol concentration led to a reduction in degradation efficiency, with a marked drop

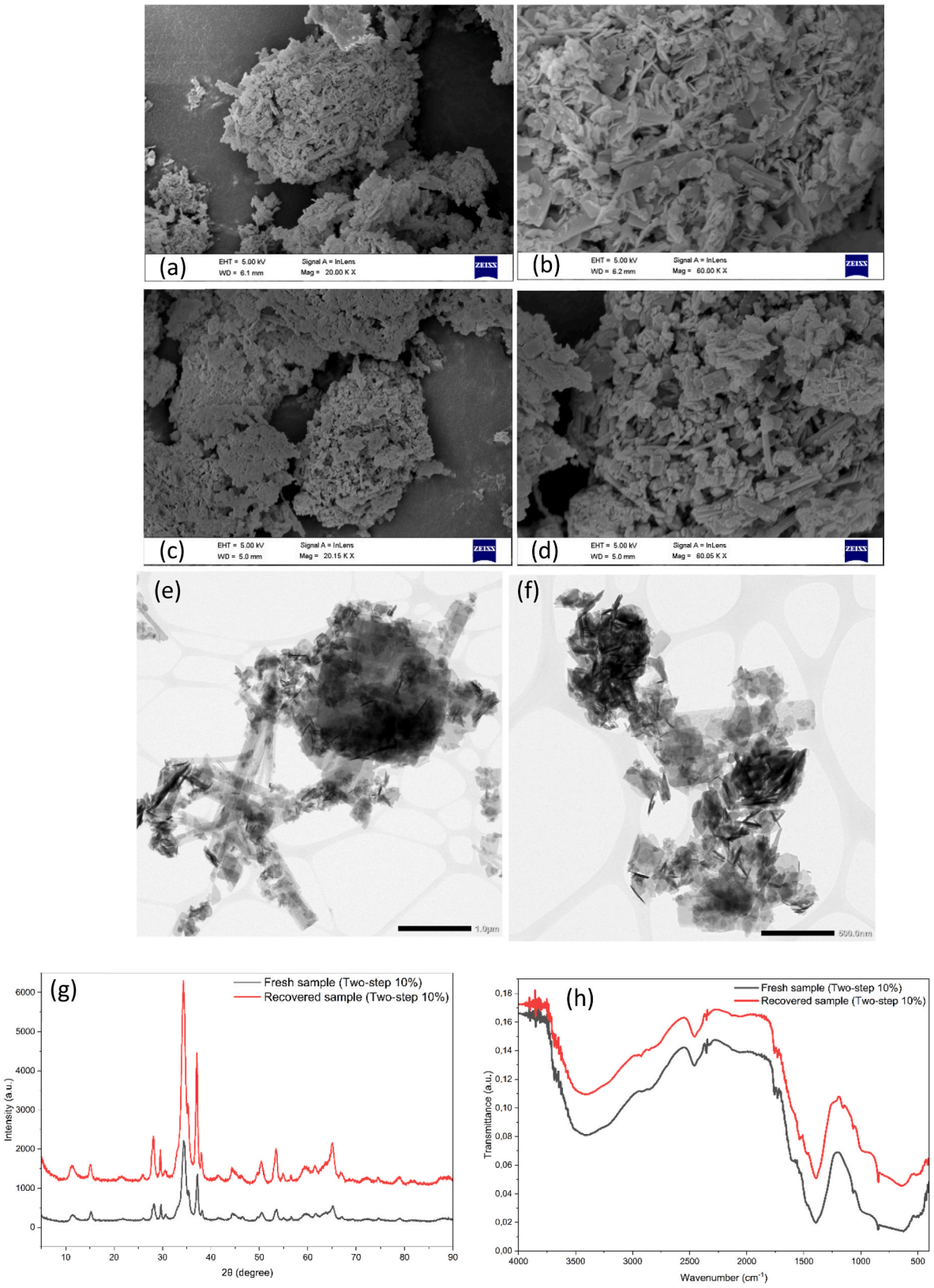

Fig. 15. FESEM images of (a-b) fresh and (c-d) recovered two-step 10%, TEM image of (e) fresh and (f) recovered two-step 10%, (g) XRD results and (h) FTIR results of fresh and recovered two-step 10% photocatalyst.

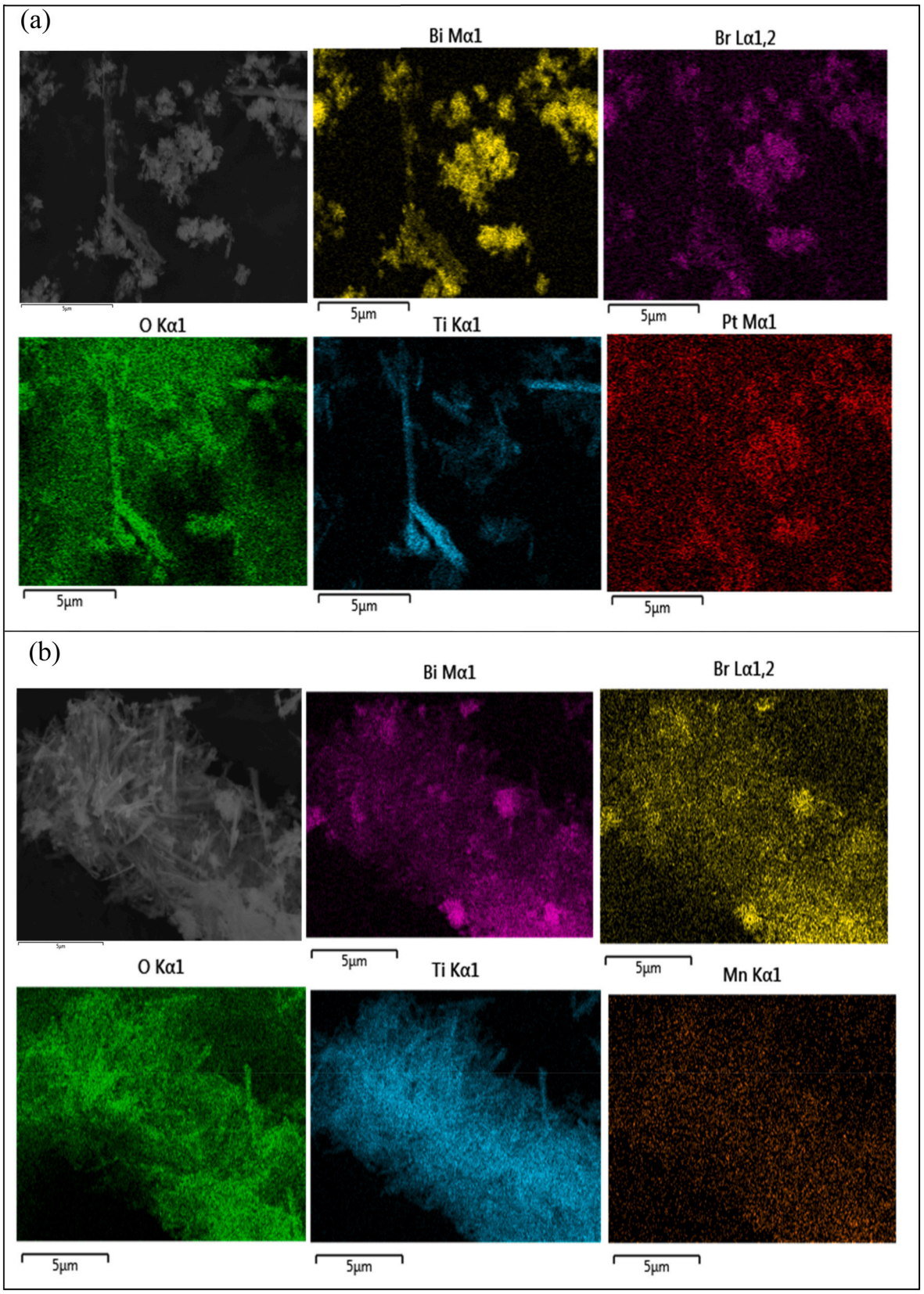

Fig. 16. Corresponding EDX elemental mapping of (a) Pt and (b) MnO_x photo-deposition on Bi_3O_4Br/TiO_2 NB/hydrochar.

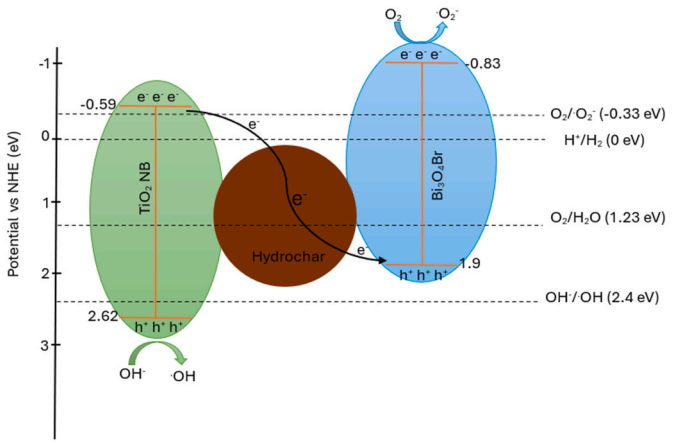

Fig. 17. Proposed photocatalytic mechanism for Bi_3O_4Br/TiO_2 NB/hydrochar photocatalyst.

observed at 20 mg L^{-1} of paracetamol. Also, higher photocatalyst dosages and temperatures enhanced degradation performance. Scavenger and EPR analyses confirmed that all photocatalysts could generate reactive oxygen species under visible light. Photogenerated holes were the dominant reactive species in paracetamol degradation, with superoxide radicals also playing a significant role and hydroxyl radicals contributing to a lesser extent. Moreover, selective photo-deposition of Pt and MnO_x provided additional evidence for a Z-scheme mechanism. The photocatalyst remained active after five cycles of reaction and reached partial mineralization of real pharmaceutical wastewater samples.

Declaration of Generative AI in the writing process

At the final stage of the writing process, the authors used ChatGPT for the language check to improve the readability of the manuscript. After using this tool, the authors reviewed and edited the content again as needed and take full responsibility for the content of the article.

CRediT authorship contribution statement

Sajad Ahmadi: Conceptualization, Data curation, Investigation, Methodology, Validation, Visualization, Writing – original draft. **Antonio Alonso:** Investigation, Methodology, Validation, Writing – review & editing. **Velma Beri Kimbi Yaah:** Supervision, Validation, Writing – review & editing. **Sergio Botelho de Oliveira:** Conceptualization, Supervision, Validation, Writing – review & editing. **Rafal Sliz:** Investigation, Methodology, Validation, Writing – review & editing. **Satu Ojala:** Funding acquisition, Project administration, Resources, Supervision, Validation, Writing – review & editing.

Declaration of competing interest

The authors declare that they have no known competing financial interests or personal relationships that could have appeared to influence the work reported in this paper.

Acknowledgements

Sajad Ahmadi would like to acknowledge Tauno Tönning Foundation for the encouragement grant. Velma Beri Kimbi Yaah acknowledges the European Union under Horizon Europe (project 101159721). Satu Ojala acknowledges financial support from Research Council of Finland and University of Oulu through H_2 Future profilation funding (352788). Some of the characterization work was supported by the Centre for Material Analysis at the University of Oulu. The authors gratefully acknowledge Anne Heponiemi and the Sustainable Chemistry research unit for providing the TOC analysis. Kaisu Ainassaari is also acknowledged for performing the BET analysis. Sami Saukko and Dr. Roya Khalili are acknowledged for their help in performing TEM. Razieh Pirouz Chaleshtori is acknowledged for her help in conducting XRD. Markus Väyrynen is acknowledged for his help in conducting ICP-MS.

Appendix A. Supplementary data

Supplementary data to this article can be found online at https://doi.org/10.1016/j.jenvman.2026.130074.

Data availability

Data will be made available on request.

References

Abdul-Raheem, M.N., Saheed, I.O., Ibrahim, M.L., Chayed, N.F., Hassan, O.H., Adnan, R., Sagadevan, S., Kaus, N.H.M., 2025. Novel BiOBr/Biochar/g-C3N4 ternary s-scheme heterojunction for enhanced visible-light photocatalytic degradation of ciprofloxacin in aqueous solutions. Surf. Interfaces 78, 108045. https://doi.org/10.1016/j.surfin.2025.108045.

Ahmadi, M., Alavi, S.M., Larimi, A., 2024a. Highly active platinum decorated BiVO4 nanosheet/TiO2 nanobelt heterojunction for photocatalytic CO2 reduction. Surf. Interfaces 45, 103908. https://doi.org/10.1016/j.surfin.2024.103908.

Ahmadi, S., Yaah, V.B.K., Asikainen, K., Ameur, S., Sliz, R., de Oliveira, S.B., Alatalo, M., Brahmi, R., Ojala, S., 2024b. Enhanced visible-light activity of bismuth-rich oxybromide photocatalysts: focus on synthesis, characterization, and modeling. J. Environ. Chem. Eng. 12, 114319. https://doi.org/10.1016/j.jece.2024.114319.

Ahmadi, S., Yaah, V.B.K., de Oliveira, S.B., Ojala, S., 2025a. A comprehensive review on the synthesis of Bi3O4Br and Bi24O31Br10 photocatalysts and their environmental applications. J. Clean. Prod. 523, 146456. https://doi.org/10.1016/j.jclepro.2025.146456.

Ahmadi, S., Yaah, V.B.K., Sliz, R., de Oliveira, S.B., Leyva-Pérez, A., Heponiemi, A., Ojala, S., 2025b. 2D/1D Z-scheme heterojunction of Bi3O4Br and TiO2 nanobelt for photocatalytic degradation of pharmaceuticals. Chem. Eng. J., 167496 https://doi.org/10.1016/j.cej.2025.167496.

Ahmed, M.E., Khajah, M., Abdullah, H., Al-Yaseen, R., 2025. Treatment of industrial wastewater of variable quality using ultrasound irradiation. Civil Eng. J. (Iran) 11, 1476–1491. https://doi.org/10.28991/CEJ-2025-011-04-013.

AlJerf, A., Maad, A.H., Ukaogo, P.O., Aljerf, L., Ajong, A.B., Alajlani, M., 2026. Antimicrobial armageddon: the professional guide to conquering antibiotic resistance. Probiotics Antimicrob. Proteins. https://doi.org/10.1007/s12602-026-10928-9.

Aljerf, L., 2018a. Data of thematic analysis of farmer's use behavior of recycled industrial wastewater. Data Brief 21, 240–250. https://doi.org/10.1016/j.dib.2018.09.125.

Aljerf, L., 2018b. High-efficiency extraction of bromocresol purple dye and heavy metals as chromium from industrial effluent by adsorption onto a modified surface of zeolite: kinetics and equilibrium study. J. Environ. Manag. 225, 120–132. https://doi.org/10.1016/j.jenvman.2018.07.048.

Alonso, L., Sampaio, R.N., Souza, T.F.M., Silva, R.C., Neto, N.M.B., Ribeiro, A.O., Alonso, A., Gonçalves, P.J., 2016. Photodynamic evaluation of tetracarboxy-phthalocyanines in model systems. J. Photochem. Photobiol., B 161, 100–107. https://doi.org/10.1016/j.jphotobiol.2016.05.008.

Asghar, H., Hermosilla, D., Gascó, A., Maurino, V., Iqbal, M.A., 2025. Exploring the photocatalytic efficiency of heterostructured TiO2 nanobelts for emerging liquid contaminants in different water matrices. Separations 12. https://doi.org/10.3390/separations12020049.

Bertagna Silva, D., Marques, A.C., 2025. TiO_2-based photocatalytic degradation of microplastics in water: current status, challenges and future perspectives. J. Water Proc. Eng. 72, 107465. https://doi.org/10.1016/j.jwpe.2025.107465.

Bi, X., Du, G., Kalam, A., Sun, D., Zhao, W., Yu, Y., Su, Q., Xu, B., Al-Sehemi, A.G., 2021. Constructing anatase TiO2/Amorphous Nb2O5 heterostructures to enhance photocatalytic degradation of acetaminophen and nitrogen oxide. J. Colloid Interface Sci. 601, 346–354. https://doi.org/10.1016/j.jcis.2021.05.120.

Cako, E., Dudziak, S., Głuchowski, P., Trykowski, G., Pisarek, M., Fiszka Borzyszkowska, A., Sikora, K., Zielińska-Jurek, A., 2023. Heterojunction of (P, S) co-doped g-C3N4 and 2D TiO2 for improved carbamazepine and acetaminophen photocatalytic degradation. Sep. Purif. Technol. 311, 123320. https://doi.org/10.1016/j.seppur.2023.123320.

Chau, J.H.F., Lai, C.W., Leo, B.F., Juan, J.C., Johan, M.R., 2022. Advanced photocatalytic degradation of acetaminophen using Cu2O/WO3/TiO2 ternary composite under solar irradiation. Catal. Commun. 163, 106396. https://doi.org/10.1016/j.catcom.2022.106396.

Chen, N., Zhang, X., Xu, Y., Hao, Z., Zhu, L., Jia, H., 2025. Bicarbonate boosts the anaerobic generation of reactive oxygen species by hydrochar: surface oxygenated functional groups activation and hexavalent chromium removal. Water Res. 281, 123727. https://doi.org/10.1016/j.watres.2025.123727.

Chen, Q., Wang, K., Gao, G., Ren, J., Duan, R., Fang, Y., Hu, X., 2021. Singlet oxygen generation boosted by Ag–Pt nanoalloy combined with disordered surface layer over

TiO2 nanosheet for improving the photocatalytic activity. Appl. Surf. Sci. 538, 147944. https://doi.org/10.1016/j.apsusc.2020.147944.
Cheng, D., Li, Y., Yang, L., Luo, S., Yang, L., Luo, X., Luo, Y., Li, T., Gao, J., Dionysiou, D. D., 2019. One–step reductive synthesis of Ti3+ self–doped elongated anatase TiO2 nanowires combined with reduced graphene oxide for adsorbing and degrading waste engine oil. J. Hazard. Mater. 378, 120752. https://doi.org/10.1016/j.jhazmat.2019.120752.
Dong, W., Qi, K., Zhang, L., Xie, X., Hu, J., Mao, M., Wang, Z., Yang, B., 2025. Synthesis of hydrochar-based AgBr/Bi2WO6 heterojunction photocatalyst using dopant element and its loading on PVDF membrane: study on degradation of sulfadiazine. Sep. Purif. Technol. 360, 131132. https://doi.org/10.1016/j.seppur.2024.131132.
Dung NT, Tung TT, Son LT, Thu TV, Nam NH, Nhi BD, Huy NN. Bimetallic zeolitic imidazolate framework (Ni/Co-ZIF) on coffee husk hydrochar to activate peroxymonosulfate for organic pollutant degradation. Vietnam J. Chem. n/a. https://doi.org/https://doi.org/10.1002/vjch.70126.
Fan, J., Bai, M., Zhang, H., Chu, Y., 2023. Synthesis and immobilization of HC/BiVO4 catalyst particles with PTFE for photocatalytic tetracycline degradation: preparation, performance and mechanism. J. Water Proc. Eng. 56, 104474. https://doi.org/10.1016/j.jwpe.2023.104474.
Feng, X., Gu, L., Wang, N., Pu, Q., Liu, G., 2023. Fe/N co-doped nano-TiO2 wrapped mesoporous carbon spheres for synergetically enhanced adsorption and photocatalysis. J. Mater. Sci. Technol. 135, 54–64. https://doi.org/10.1016/j.jmst.2022.06.038.
Gonçalves, P.J., Bezzerra, F.C., Teles, A.V., Menezes, L.B., Alves, K.M., Alonso, L., Alonso, A., Andrade, M.A., Borissevitch, I.E., Souza, G.R.L., Iglesias, B.A., 2020. Photoinactivation of Salmonella enterica (serovar Typhimurium) by tetra-cationic porphyrins containing peripheral [Ru(bpy)2Cl]+ units. J. Photochem. Photobiol. Chem. 391, 112375. https://doi.org/10.1016/j.jphotochem.2020.112375.
Guan, W., Li, Y., Zhong, Q., Liu, H., Chen, J., Hu, H., Lv, K., Gong, J., Xu, Y., Kang, Z., Cao, M., Zhang, Q., 2021. Fabricating MAPbI3/MoS2 composites for improved photocatalytic performance. Nano Lett. 21, 597–604. https://doi.org/10.1021/acs.nanolett.0c04073.
Hansen, L., Hack, U., Rizzana, D.U., Siqueira, M.A.R., Weibel, D.E., 2025. Synthesis and characterization of a semiconducting CeO2 – SnO2 hybrid via a greener novel solid-state chemistry route and its performance in the degradation of paracetamol in water. J. Alloys Compd. 1044, 184559. https://doi.org/10.1016/j.jallcom.2025.184559.
Hassan, F., Backer, S.N., Almanassra, I.W., Ali Atieh, M., Elbahri, M., Shanableh, A., 2024. Solar-matched S-scheme ZnO/g-C3N4 for visible light-driven paracetamol degradation. Sci. Rep. 14, 12220. https://doi.org/10.1038/s41598-024-60306-0.
Hosny, M., Fawzy, M., Eltaweil, A.S., 2022. Green synthesis of bimetallic Ag/ZnO@Biohar nanocomposite for photocatalytic degradation of tetracycline, antibacterial and antioxidant activities. Sci. Rep. 12, 7316. https://doi.org/10.1038/s41598-022-11014-0.
Imam, S.S., Adnan, R., Kaus, N.H.M., 2018. Influence of yttrium doping on the photocatalytic activity of bismuth oxybromide for ciprofloxacin degradation using indoor fluorescent light illumination. Res. Chem. Intermed. 44, 5357–5376. https://doi.org/10.1007/s11164-018-3427-8.
Imam, S.S., Adnan, R., Mohd Kaus, N.H., Hussin, M.H., 2019. Room-temperature synthesis of Bi/BiOBr composites for the catalytic degradation of ciprofloxacin using indoor fluorescent light illumination. J. Mater. Sci. Mater. Electron. 30, 6263–6276. https://doi.org/10.1007/s10854-019-00930-z.
Janus, M., Kusiak-Nejman, E., Morawski, A.W., 2012. Influence of water temperature on the photocatalytic activity of titanium dioxide. React. Kinet. Mech. Catal. 106, 289–295. https://doi.org/10.1007/s11144-012-0432-6.
Ju, P., Yu, S., Zhang, G., Mou, H., Wang, J., Li, Y., Lu, S., Sun, J., 2025. Spartina alterniflora biochar coupled BiOBr with dominant exposed facet and oxygen vacancies for efficiently photocatalytic degradation of ciprofloxacin. Colloids Surf. A Physicochem. Eng. Asp. 711, 136306. https://doi.org/10.1016/j.colsurfa.2025.136306.
Kaur, S., Pal, B., 2025. Au nanoparticles decorated upon TiO2/ZnO-nanoflower hybrids for the enhanced visible-light-induced photocatalytic degradation of paracetamol. J. Water Proc. Eng. 75, 108046. https://doi.org/10.1016/j.jwpe.2025.108046.
Khodadadian, F., de Boer, M.W., Poursaeidesfahani, A., van Ommen, J.R., Stankiewicz, A.I., Lakerveld, R., 2018. Design, characterization and model validation of a LED-based photocatalytic reactor for gas phase applications. Chem. Eng. J. 333, 456–466. https://doi.org/10.1016/j.cej.2017.09.108.
Kimbi Yaah, V.B., Quimbayo, J.S.M., Ahmadi, S., Lempelto, A., Sliz, R., Cao, W., Pastrana-Martínez, L.M., Maldonado-Hódar, F.J., Morales-Torres, S., 2025. One-pot co-precipitation of enhanced visible light active BiOCl based photocatalysts: characterization, mechanism and DFT modelling. Inorg. Chem. Commun. 182, 115699. https://doi.org/10.1016/j.inoche.2025.115699.
Kuk, S.K., Ji, S.M., Kang, S., Yang, D.S., Kwon, H.J., Koo, M.S., Oh, S., Lee, H.C., 2023. Singlet-oxygen-driven photocatalytic degradation of gaseous formaldehyde and its mechanistic study. Appl. Catal., B 328, 122463. https://doi.org/10.1016/j.apcatb.2023.122463.
Li, L., Ye, F., Lv, Q., Xia, J., Chen, N., Wang, H., Chen, L., Zhao, K., Zeng, Z., Ahmad, M., Xiao, Z., Wang, S., Zhang, Q., 2025b. Polydopamine-coated hollow carbon nitride as a full-spectral response photocatalyst for efficient H2O2 production via redox dual pathways. Appl. Catal. B Environ. Energy 363, 124802. https://doi.org/10.1016/j.apcatb.2024.124802.
Li, Q., Zhou, H., Li, Z., Liu, A., Wang, E., Wu, Y., Tang, X., Du, H., Jin, L., Zhu, H., Ni, B., Wang, Q., 2025a. Efficient photocatalytic degradation of antibiotics using Z-scheme MIL-88(Fe)/Ti3C2/MoO3: mechanistic insights and toxicity assessment. J. Hazard. Mater. 486, 137051. https://doi.org/10.1016/j.jhazmat.2024.137051.
Li, S., Ma, Q., Chen, L., Yang, Z., Aqeel Kamran, M., Chen, B., 2022. Hydrochar-mediated photocatalyst Fe3O4/BiOBr@HC for highly efficient carbamazepine degradation under visible LED light irradiation. Chem. Eng. J. 433, 134492. https://doi.org/10.1016/j.cej.2021.134492.
Li, S., Wang, Z., Xie, X., Liang, G., Cai, X., Zhang, X., Wang, Z., 2020. Fabrication of vessel–like biochar–based heterojunction photocatalyst Bi2S3/BiOBr/BC for diclofenac removal under visible LED light irradiation: mechanistic investigation and intermediates analysis. J. Hazard. Mater. 391, 121407. https://doi.org/10.1016/j.jhazmat.2019.121407.
Li, Y., Gao, X., Li, Y., 2024. Strategic pathway selection for photocatalytic degradation: roles of holes and radicals. Inorg. Chem. Front. 11, 8183–8211. https://doi.org/10.1039/D4QI01635A.
Lin, C., Fan, G., Luo, J., Cai, C., Cao, X., Xu, K.-Q., 2025. Synergistic piezoelectric effect and oxygen vacancies in MoS2/BiOIO3 heterojunctions boosting photocatalytic degradation of 17β-estradiol. Chem. Eng. J. 520, 166094. https://doi.org/10.1016/j.cej.2025.166094.
Liu, S., Ke, J., Sun, H., Liu, J., Tade, M.O., Wang, S., 2017. Size dependence of uniformed carbon spheres in promoting graphitic carbon nitride toward enhanced photocatalysis. Appl. Catal., B 204, 358–364. https://doi.org/10.1016/j.apcatb.2016.11.048.
Maad, A.H., Alajlani, M., Choukaife, H., Aljerf, L., 2026. Phytosynthesis of zinc oxide nanoparticles using Thymus vulgaris leaf extract: characterization and dual biological efficacy. Results Chem. 23, 103173. https://doi.org/10.1016/j.rechem.2026.103173.
Makuła, P., Pacia, M., Macyk, W., 2018. How to correctly determine the band gap energy of modified semiconductor photocatalysts based on UV–Vis spectra. J. Phys. Chem. Lett. 9, 6814–6817. https://doi.org/10.1021/acs.jpclett.8b02892.
Meng, M., Zhou, H., Liu, W., Yang, J., Yuan, H., Gan, Z., 2025. Three-dimensional TiO2 nanobelt array with a disordered surface and oxygen vacancies for boosted photoelectrochemical water splitting. New J. Chem. 49, 886–892. https://doi.org/10.1039/D4NJ03722G.
Michel, J., Silva, S., Joazet, H., Galván, O., Giovanny, E., Leal, V., Judith, G., Delgado, L., Alejandro, S., Maruri, A., Fuentes, R., 2024. Synergistic Photocatalysis of a Hydrochar/Ceo 2 Composite for Dye Degradation Under Visible Light, pp. 16453–16472.
Mohsentabar, A., Amooey, A.A., Ghasemi, S., Azizzadeh, A., 2023. Enhanced photocatalytic degradation of acetaminophen from aqueous solution using Ag/ZnO nanoparticles. Results Chem. 6, 101200. https://doi.org/10.1016/j.rechem.2023.101200.
Mukheef, R.A.H., Hassan, W.H., Alquzweeni, S., 2024. Artificial recharge of an unconfined aquifer using treated wastewater as a climate change mitigation strategy. Civil Eng. J. (Iran) 10, 319–343. https://doi.org/10.28991/CEJ-SP2024-010-016.
Nannou, C., Maroulas, K.N., Tsamtzidou, C., Ladomenou, K., Kyzas, G.Z., 2025. Photocatalytic degradation of veterinary antibiotics in wastewaters: a review. Sci. Total Environ. 966, 178765. https://doi.org/10.1016/j.scitotenv.2025.178765.
Niu, J., Guo, X., Zhang, Y., Yu, X., Yao, B., 2025. Construction of Z-scheme Bi3O4Br/BiVO4 nanocomposites as a promising photocatalyst for organic pollutant degradation. J. Alloys Compd. 1031, 181041. https://doi.org/10.1016/j.jallcom.2025.181041.
Niu, Z., Chen, C., Yin, Z., Zhang, X., Sun, J., Shi, H., 2026. Mechanism insight into the Fe3O4/biochar/BiOBr S–scheme heterostructure with improved photocatalytic degradation performance for pharmaceutical wastewater. Colloids Surf. A Physicochem. Eng. Asp. 728, 138518. https://doi.org/10.1016/j.colsurfa.2025.138518.
Nor, N.U.M., Amin, N.A.S., 2019. Glucose precursor carbon-doped TiO2 heterojunctions for enhanced efficiency in photocatalytic reduction of carbon dioxide to methanol. J. CO2 Util. 33, 372–383. https://doi.org/10.1016/j.jcou.2019.07.002.
Parida, V.K., Srivastava, S.K., Chowdhury, S., Gupta, A.K., 2023. Facile synthesis of 2D/0D Bi2O3/MnO2 Z-scheme heterojunction for enhanced visible light-assisted photocatalytic degradation of acetaminophen. Chem. Eng. J. 472, 144969. https://doi.org/10.1016/j.cej.2023.144969.
Puri, S., Thakur, I., Verma, A., Barman, S., 2021. Degradation of pharmaceutical drug paracetamol via UV irradiation using Fe-TiO2 composite photocatalyst: statistical analysis and parametric optimization. Environ. Sci. Pollut. Control Ser. 28, 47327–47341. https://doi.org/10.1007/s11356-021-13895-6.
Qi, K., Wang, Z., Xie, X., Wang, Z., 2023. Photocatalytic performance of pyrochar and hydrochar in heterojunction photocatalyst for organic pollutants degradation: activity comparison and mechanism insight. Chem. Eng. J. 467, 143424. https://doi.org/10.1016/j.cej.2023.143424.
Quimbayo, J.S., Kimbi Yaah, V.B., Ahmadi, S., Fenandez-Catalá, J., de Oliveira, S.B., Ojala, S., 2025. Using TiO2 in photocatalytic reactors: vocs, NOx, CO2 removal and H2 production. Appl. Surf. Sci. Adv. 30, 100886. https://doi.org/10.1016/j.apsadv.2025.100886.
Ren, S., Usman, M., Tsang, D.C.W., O-Thong, S., Angelidaki, I., Zhu, X., Zhang, S., Luo, G., 2020. Hydrochar-facilitated anaerobic digestion: evidence for direct interspecies electron transfer mediated through surface oxygen-containing functional groups. Environ. Sci. Technol. 54, 5755–5766. https://doi.org/10.1021/acs.est.0c00112.
Sánchez-Silva, J.M., Ojeda-Galván, H.J., Villabona-Leal, E.G., Labrada-Delgado, G.J., Aguilar-Maruri, S.A., Fuentes-Ramírez, R., González-Ortega, O., López-Ramón, M.V., Ocampo-Pérez, R., 2024. Synergistic photocatalysis of a hydrochar/CeO2 composite for dye degradation under visible light. Environ. Sci. Pollut. Control Ser. 31, 16453–16472. https://doi.org/10.1007/s11356-024-32281-6.
Sun, L., He, X., Liu, B., Zhang, S., Xiang, Z., Wang, X., Wang, Y., 2025. Synergistic adsorption-photocatalytic degradation of tetracycline by S-scheme InVO4/ZnIn2S4

heterojunction: mechanism, toxicity assessment, and potential applications. Sep. Purif. Technol. 353, 128515. https://doi.org/10.1016/j.seppur.2024.128515.
Tabieh, M.A., Al-Karablieh, E.K., Qtaishat, T.H., Salman, A.Z., Thaher, N.H., Al-Karablieh, N.K., Al-Jaghbir, M.T., Al-Zghoul, T.M., Jamrah, A.I., 2025. Assessment of fresh water reallocation by treated wastewater for irrigation. HighTech Innov. J. 6, 236–256. https://doi.org/10.28991/HIJ-2025-06-01-016.
Thi, V.H.-T., Lee, B.-K., 2017. Effective photocatalytic degradation of paracetamol using La-doped ZnO photocatalyst under visible light irradiation. Mater. Res. Bull. 96, 171–182. https://doi.org/10.1016/j.materresbull.2017.04.028.
Wang, C., Liu, N., Zhao, X., Tian, Y., Chen, X., Zhang, Y., Fan, L., Hou, B., 2023. C-doped BiOCl/Bi2S3 heterojunction for highly efficient photoelectrochemical detection and photocatalytic reduction of Cr(VI). J. Mater. Sci. Technol. 164, 188–197. https://doi.org/10.1016/j.jmst.2023.03.066.
Wang, D., Jia, F., Wang, H., Chen, F., Fang, Y., Dong, W., Zeng, G., Li, X., Yang, Q., Yuan, X., 2018. Simultaneously efficient adsorption and photocatalytic degradation of tetracycline by Fe-based MOFs. J. Colloid Interface Sci. 519, 273–284. https://doi.org/10.1016/j.jcis.2018.02.067.
Wang, Q., Peng, Y., He, A., Li, Z., Jia, J., Xu, H., Yu, Y., Zhang, Z., 2025. A well-constructed Bi3O4Br/PANI composite: elevation of visible-light photocatalytic degradation performance through the synergistic mechanism of oxygen vacancies and heterojunctions. Surf. Interfaces 70, 106866. https://doi.org/10.1016/j.surfin.2025.106866.
Wu, H., Jing, J., Li, S., Li, S., Liu, J., Liang, R., Zhang, Y., Xia, Z., Zhou, M., 2025. Novel discrete architecture for quantum dots modified ultrathin hollow nanotube Bi2Sn2O7/Bi4O5I2 S-scheme heterojunction for ultra-efficient photocatalytic degradation of bisphenol A. Appl. Catal. B Environ. Energy 360, 124517. https://doi.org/10.1016/j.apcatb.2024.124517.
Wu, S., Hu, H., Lin, Y., Zhang, J., Hu, Y.H., 2020. Visible light photocatalytic degradation of tetracycline over TiO2. Chem. Eng. J. 382, 122842. https://doi.org/10.1016/j.cej.2019.122842.
Wu, S., Li, X., Tian, Y., Lin, Y., Hu, Y.H., 2021. Excellent photocatalytic degradation of tetracycline over black anatase-TiO2 under visible light. Chem. Eng. J. 406, 126747. https://doi.org/10.1016/j.cej.2020.126747.
Xu, L., Li, L., Yu, L., Yu, J.C., 2022. Efficient generation of singlet oxygen on modified g-C3N4 photocatalyst for preferential oxidation of targeted organic pollutants. Chem. Eng. J. 431, 134241. https://doi.org/10.1016/j.cej.2021.134241.
Yadav, S., Priyadarshini, M., Ahmad, A., Ghangrekar, M.M., Dubey, B.K., 2024. Food-waste-derived hydrochar to a low-cost p-type semiconducting photocatalyst (Zn–Al@HC): multifunctional role in real wastewater treatment and environmental sustainability. J. Mater. Chem. A 12, 15240–15253. https://doi.org/10.1039/D4TA00460D.
Yang, C., Zhong, H., Wang, T., Ji, X., Deng, J., Hu, X., Tang, C., Tan, X., Xu, X., 2025. High molecular oxygen activation capacity of carbon defective g-C3N5 for photocatalytic degradation of antibiotics in water. Sep. Purif. Technol. 354, 128928. https://doi.org/10.1016/j.seppur.2024.128928.
Yang, Q., Li, X., Tian, Q., Pan, A., Liu, X., Yin, H., Shi, Y., Fang, G., 2023. Synergistic effect of adsorption and photocatalysis of BiOBr/lignin-biochar composites with oxygen vacancies under visible light irradiation. J. Ind. Eng. Chem. 117, 117–129. https://doi.org/10.1016/j.jiec.2022.09.044.
Ye, F., Liu, Y., Lv, Q., Gao, B., Xia, J., Li, X., Dou, M., Zhao, K., Ahmad, M., Xiao, Z., Wang, S., Wang, S., Zhang, Q., 2026. Unveiling the mechanism of efficient detoxification by Pd species in chlorinated pollutant degradation. Chin. Chem. Lett. 37, 111136. https://doi.org/10.1016/j.cclet.2025.111136.
Ye, F., Qian, J., Xia, J., Li, L., Wang, S., Zeng, Z., Mao, J., Ahamad, M., Xiao, Z., Zhang, Q., 2024. Efficient photoelectrocatalytic degradation of pollutants over hydrophobic carbon felt loaded with Fe-doped porous carbon nitride via direct activation of molecular oxygen. Environ. Res. 249, 118497. https://doi.org/10.1016/j.envres.2024.118497.
Zeinali, Heris S., Bagheri Khaniani, P., Mousavi, S.B., 2025. Photocatalytic degradation of co-amoxiclav using hybrid TiO2/ZnO nanoparticles: experimental and optimization. J. Water Proc. Eng. 70, 107040. https://doi.org/10.1016/j.jwpe.2025.107040.
Zhang, F., Liu, C., Wang, S., Zhang, Y., 2025b. Fabricating efficient SnO 2/hydrochar heterojunction visible light photocatalyst for Cr (VI) reduction. J. Mol. Struct. 1336, 142084. https://doi.org/10.1016/j.molstruc.2025.142084.
Zhang, J., Xie, J.-F., Yang, J.-C.E., Li, D., Zhong, L.-B., Zheng, Y.-M., 2023. Ultra-fast degradation of ciprofloxacin by the peroxymonosulfate activation using a Co/Al-LDH decorated magnetic hydrochar: structural design, catalytic performance and synergistic effects. Chem. Eng. J. 477, 146961. https://doi.org/10.1016/j.cej.2023.146961.
Zhang, Y., Liu, C., Nian, P., Ma, H., Hou, J., Zhang, Y., 2024. Facile preparation of high-performance hydrochar/TiO2 heterojunction visible light photocatalyst for treating Cr(VI)-polluted water. Colloids Surf. A Physicochem. Eng. Asp. 681, 132775. https://doi.org/10.1016/j.colsurfa.2023.132775.
Zhang, Y., Yuan, L., Deng, Q., Li, R., Yin, X., Bao, T., Zhang, T., Luo, S., Yang, R., 2025a. Construction of S-scheme heterojunction photocatalyst ZnO/Bi3O4Br for efficient removal of tetracycline and dye contaminants under visible illumination. Mater. Sci. Semicond. Process. 199, 109873. https://doi.org/10.1016/j.mssp.2025.109873.
Zhao, C., Li, W., Liang, Y., Tian, Y., Zhang, Q., 2016. Synthesis of BiOBr/carbon quantum dots microspheres with enhanced photoactivity and photostability under visible light irradiation. Appl. Catal. Gen. 527, 127–136. https://doi.org/10.1016/j.apcata.2016.09.005.
Zhao, H., Greco, R., Sliz, R., Pitkänen, O., Kordas, K., Ojala, S., 2024. Interfacial linkage modulated amorphous molybdenum sulfide/bismuth halide perovskite heterojunction for enhanced visible-light-driven photocatalytic hydrogen evolution. Appl. Catal. B Environ. Energy 358, 124454. https://doi.org/10.1016/j.apcatb.2024.124454.
Zhou, L., Cai, M., Zhang, X., Cui, N., Chen, G., Zou, G., 2019. Key role of hydrochar in heterogeneous photocatalytic degradation of sulfamethoxazole using Ag3PO4-based photocatalysts. RSC Adv. 9, 35636–35645. https://doi.org/10.1039/C9RA07843F.
Zhou, Y., Deng, H., Li, Z., Wang, Y., Ma, T., 2023. Construction of CuBi2O4/BiOBr/biochar Z-scheme heterojunction for degradation of gaseous benzene under visible light. Catal. Lett. 153, 2319–2330. https://doi.org/10.1007/s10562-022-04071-7.